STUDIES ON CONTRAST ENHANCED MICROCOMPUTED TOMOGRAPHY IMAGING

A THESIS SUBMITTED

BY

MEENU RAJENDRAN

IN PARTIAL FULFILLMENT OF THE REQUIREMENTS

FOR THE DEGREE OF

MASTER OF PHILOSOPHY

SREE CHITRA TIRUNAL INSTITUTE
FOR MEDICAL SCIENCES AND TECHNOLOGY
THIRUVANANTHAPURAM – 695 012

DECLARATION

I, **Meenu Rajendran**, hereby declare that I had personally carried out the work depicted in the thesis entitled "**Studies on Contrast Enhanced Microcomputed tomography Imaging**" under the direct supervision of **Dr. V. Kalliyana Krishnan, Scientist In Charge, Dental Products Laboratory,** Biomedical Technology Wing, Sree Chitra Tirunal Institute for Medical Sciences and Technology, Thiruvananthapuram, Kerala, India. External help sought are acknowledged.

Meenu R.

Meenu Rajendran

SREE CHITRA TIRUNAL INSTITUTE
FOR MEDICAL SCIENCES & TECHNOLOGY
THIRUVANANTHAPURAM – 695011, INDIA
(An Institute of National Importance under Govt. of India)

CERTIFICATE

This is to certify that the dissertation entitled "**Studies on Contrast Enhanced Microcomputed tomography Imaging**" submitted by **Meenu Rajendran** in partial fulfilment for the degree of Master of Philosophy in Biomedical Technology to be awarded by this Institute. The entire work was done by her under my supervision and guidance at **Dental Products Laboratory**, Biomedical Technology Wing, Sree Chitra Tirunal Institute for Medical Sciences and Technology (SCTIMST), Thiruvananthapuram-695012.

Thiruvananthapuram

Date: 10th August 2010

Dr.Kalliyana Krishnan.V

The Thesis

Entitled

STUDIES ON CONTRAST ENHANCED MICROCOMPUTED TOMOGRAPHY IMAGING

Submitted
by

Meenu Rajendran

For

Master of Philosophy

Of

SREE CHITRA TIRUNAL INSTITUTE FOR MEDICAL SCIENCES AND TECHNOLOGY

THIRUVANANTHAPURAM

Evaluated and approved

By

Signature

M. V. Kalliyana Krishnan.
Name of Supervisor

Signature 20/08/2010

DR. C. KESAVADAS.
Examiners name and designation

Acknowledgements

I wish to thank Prof. K. Radhakrishnan, Director, SCTIMST and Dr. G. S. Bhuvaneshwar, Head, Biomedical Technology Wing, SCTIMST, for giving me this opportunity to carry out my MPhil research project and for providing all the facilities.

I also wish to express my deep sense of gratitude to Dr. V. Kalliyana Krishnan., Scientist G & Scientist-in-Charge, Dental Products Lab, SCTIMST for his valuable guidance and encouragement throughout the course of this work.

I am indebted to all the help provided to me by Mr. S. Jayasingh, Deputy Registrar, SCTIMST, Mr. Renjith and Ms. Prathiba of the academic division throughout the course of the project.

I convey my sincere thanks to Dr. Lissy K. Krishnan, Dr. Asha S. Mathew and Dr. Diksha Painuly for their valuable advices and for providing me with facilities to carry out the biological side of the work.

My heartfelt thanks to Mr. Arun Torris and Mr. R. Satheesh for their cooperation and encouragement for the successful completion of this work. Also I would like to thank all my labmates especially Ms. Rethikala, Mrs. Sreekala, Ms. Soumya, Ms. Shalini, Mr. Shyam and Mr. Rejin for their support throughout this work.

I extend my sincere thanks to all my friends of the M.Phil 2009-2010 batch for their support, joyful times and for the ever memorable days in this campus. I take this opportunity to thank my beloved ones for being with me and giving me the strength to carry out this work.

Last but not the least, I bow before "GOD Almighty", without whose help and blessings, this work would not have been a success.

Meenu Rajendran

List of Abbreviations

ADC	Analogue to Digital Converter
CAT	Computed Axial Tomography
CCD	Charged Coupled Device
2D	2-Dimensional
3D	3-Dimensional
DI	Deionised
DLS	Dynamic Light Scattering
EDTA	Ethylene Diamine Tetra Acetic acid
ESEM	Environmental Scanning Electron Microscopy
EDAX	Energy Dispersive X-ray Absorptiometry
GNP	Gold Nanoparticle
HAP	Hydroxyapatite
HUVEC	Human Umbilical Vein Endothelial Cells
IMDM	Iscove's modified Dulbecco's Minimal Essential Medium
MGG	Maygrunwald -Giemsa
Micro-CT	Micro Computed tomography
MRI	Magnetic Resonance Imaging
NSF	Nephrogenic Systemic Fibrosis
PBS	Phosphate Buffered Saline
PCL	Polycaprolactone
PEG	Polyethyleneglycol
PTA	Phosphotungstic acid

TEM	Transmission Electron Microscope
TDI	Time Delay Integration

To my Parents and
Beloved Husband

Table of Contents

List of Figures

List of Tables

Synopsis

Imaging techniques are serving an increasingly important role in the precise characterization of biomaterial properties and function. Microcomputed tomography (Micro-CT) provides rapid reconstruction of high resolution 3D images and quantitative volumetric analysis of X-ray attenuating materials or mineralized tissues. Through the use of selected contrast agents, the boundaries of quantitative micro-CT analysis can also be expanded beyond radio opaque materials to include low attenuating materials such as soft tissues. In regenerative medicine revascularization is a critical issue. The ingrowth of cells in to the polymer scaffolds can be clearly visualized using micro-CT with the aid of appropriate contrast agents. The contrast agents in use currently are mainly based on perfusion technique of autopsy samples and also they have several limitations. In the present study the spotlight is on the development of a suitable contrast enhanced micro-CT based imaging methodology for detecting the cellular infiltration on to polymer scaffolds.

Several electron microscopic stains as well as nanoscale contrast agents are presently used for micro-CT imaging of low attenuating materials; but none of these cannot contribute much to the exact issue of 3D contrast enhanced micro-CT imaging of polymer–tissue constructs. Phosphotungstic acid (PTA), a heavy metal electron microscopic stain is a choice of interest in the present study due to its easy availability, low cost and less toxicity thus facilitating easy handling. However, considering the significance of nanomaterials especially gold nanoparticle as excellent X-ray contrast enhancers, an assessment of the two will smooth the progress of developing a methodology for contrast enhanced imaging of scaffold tissue constructs.

During the first phase of the study, the contrast enhancement towards the bare PCL scaffolds by PTA and GNP were evaluated. Initially the attenuation profile of PTA is measured and different concentrations of the stain are prepared. Bare Polycaprolactone (PCL) scaffolds were incubated in different concentrations of the stain, incubated for different time periods and the attenuation histogram was plotted to

detect the optimum concentration of the stain that can provide maximum attenuation in limited incubation time. In addition, GNPs were synthesized and characterized using different techniques such as DLS, TEM, UV-VIS spectrophotometer and Fluorescence spectrophotometer. The attenuation coefficient of GNP was also measured using micro-CT. Following the characterization of the GNP, it was applied to bare PCL scaffolds (incubated for 24 hours).

X-ray attenuation of both PTA and GNP as well as their contrast enhancement property on bare PCL scaffolds were determined. The second phase starts with contrast enhancement of cell seeded PCL scaffolds using PTA and GNP. The PCL scaffolds were seeded with HUVECs and cultured in dynamic and static mode. After the culture period, the cell seeded scaffolds were stained with GNP (during the last stage of the culture) and PTA (0.3% for 16 hrs after the culture period and fixation). Also to a part of the cell seeded scaffolds, MGG staining was performed to evaluate the cell morphology on the scaffolds using light microscopic examination. The GNP and PTA stained scaffolds were then imaged using micro-CT and their voxel intensity histogram is evaluated with control specimen to obtain an optimum threshold value for isolating the datasets pertaining to cell tissue volume. The threshold value so obtained was used to reconstruct 3D images of cell volumes and quantification of cumulative cell tissue volume and its distribution profile across the scaffold. The GNP stained scaffolds were then subjected to ESEM-EDAX analysis to confirm the presence of GNP in the cells and also to detect the growth pattern of cells on the scaffolds.

PTA exhibited high linear attenuation coefficient (7.997) and also found to improve the contrast of the polymer scaffold (1 %, 4 hours). Characterization studies of GNP indicate that the particle size was around 20 nm and possessed spherical shape. The fluorescence spectrum was recorded and the emission intensity was maximum at 532 nm at an excitation of 450 nm. It is reported that for nanoparticles without surface modifications the fluorescent property is negligible or unable to detect. Therefore in the present study any fluorescence based detection methods are not applicable. The attenuation profile of GNP is similar to that of PTA (7.997), but

its contrast enhancement on bare PCL scaffold is very poor compared to that of PTA. This may be because PTA is having affinity towards functional groups such as carboxyl groups which is prominent in PCL.

Contrast enhancement studies on cell seeded scaffolds indicate that PTA stained scaffolds exhibited higher cell volume, cell tissue distribution and 3D visualization compared to GNP. Three-dimensional micro-CT images of contrast enhanced cell seeded scaffolds in dynamic and static culture modes show noticeable change in cell volume and its distribution. In both PTA and GNP stained scaffolds, dynamic culture mode exhibited prominent cell volume and distribution which is in agreement with previous studies. The light microscopic examination as well as the SEM pictures clearly visualized the cell morphology as well as the growth pattern of the cells , but the EDAX spectra was unable to record any peaks of gold nanoparticle. This may be due to the low concentration of GNP or else the prominent spectrum peaks maybe suppressing the presence of GNP.

In the present study, an appropriate method for the 3D visualization of bare polymer scaffolds as well as cell seeded scaffolds has been developed using PTA and GNP. The comparison of the contrast enhancement property of the heavy metal stain PTA and the new generation nanoscale contrast agent GNP indicates that PTA is most suited for this application than the later. The chance of modifying GNP in such a way as to improve the attenuation of bare PCL scaffolds cannot be negligible. Furthermore, GNPs can be conjugated with specific targeting moieties in order to facilitate some receptor ligand interaction with the cells there by ensuring the GNP uptake and reducing the incubation time. In future, nanoscale contrast agents that can target specific cell types will turn out to be the novel strategy for the 3D visualization of the low attenuating materials using micro-CT.

Introduction

Chapter I

Introduction

1.1. Background

Imaging has been considered as the "eyes of science". Modern imaging technologies allow for visualization of multi-dimensional and multi-parameter data. Imaging is increasingly used to measure various physical parameters as well as biological functions. It encompasses more than any one discipline or any one level of analysis. Improved spatial and temporal resolution of contemporary imaging technologies enable investigators to draw inferences about fundamental biological processes at the level of genes, cells, and organ systems, leading to a tremendous opportunity to apply imaging methods in basic biomedical research.

Biomedical imaging is a complex endeavor concerned with the presentation of multidimensional data in ways that facilitate rapid and accurate interpretation of information. Conventional techniques used in biomedical imaging comprise of optical imaging, magnetic resonance imaging and X-ray based imaging techniques.

Optical imaging is indisputably the most versatile and widely used visualization modality in clinical practice and research. Microscopy remains a diagnostic gold standard and a mostly flexible visualization tool, with new techniques continuously emerging. Even though microscopy remains the most widely used imaging technique in biomedical research, both optical and electron microscopic examination requires extensive sample preparation and slicing of the specimen. This is a serious limitation especially when unique samples have to be studied. The advent of fluorescence microscopy has been a major step forward in the study of living cells. Through the characteristic emissions of excited biological fluorophores, such as fluorescent proteins, it is possible to gain insight on cell structure and function. But the major disadvantage is the photo bleaching effect of the fluorophores which in turn limits the time that an experiment can run.

Magnetic resonance imaging is an adaptable medical imaging technology, with steadily expanding applications in clinical medicine and biomedical research. MR imaging is valued for its capability to provide high-contrast definition of normal and abnormal tissues. It also allows a freely oriented plane-of-section, making it a key tool in brain and musculoskeletal imaging and for diagnosing and staging cancer. However because of the strong magnetic field used in patients electrically, magnetically or mechanically activated implants such as cardiac pacemakers, implantable defibrillators and some artificial heart valves may not be able to have MRI safely. Patient could develop an allergic reaction to the contrasting agent, or that a skin infection could develop at the site of injection. Several reports point toward MRI contrast agents based on gadolinium to be the cause of a severe systemic disorder called Nephrogenic Systemic Fibrosis (NSF) MRI is most suitable for soft tissue imaging; whereas hard and mineralized tissues cannot be clearly visualized using MRI. This restricts the applications of the instrument in a wider perspective.

It has been more than a century since Roentgen's discovery of X-rays that initiated the modern field of biomedical imaging. X-ray computerized tomography invented by Hounsfield and Cormack in 1973 found its applications in medicine as a diagnostic device in spite of its poor spatial resolution (typically 0.3-1.00 mm). Recently principles of X-ray computed tomography were implemented in desktop microcomputed tomography (micro-CT) instruments for applications in fundamental research that is both in materials science and biomedical technology.

Micro-CT derived from Computed Axial Tomography (CAT), is a non-destructive technique, which allows high spatial resolution of inner structures to be recorded. The linear resolution of micro-CT depends on the X-ray source and scanner designs. The data can be registered both in two or three dimensions and used for qualitative or quantitative analyses. As well, the inherent image artifacts are small compared to other imaging modalities.

In the field of biomedical imaging micro-CT is a promising device. It can be adapted to evaluate both macroscopic and microscopic structures of bone. Orientation,

shape and connectivity of trabeculae can be appreciated and analysed using micro-CT. The trabecular bone strength may play an important clinical role in early predictions of osteoporosis onset. It also provides information regarding the functional pores on the ceramic related implants and can be used for the characterization of scaffold biomaterials for orthopedic application. Characterization of the internal 3-D structure of matrix-type drug delivery devices is possible with micro-CT. The CT image analysis can provide detailed quantitative information on macroporosity for correlation with formulation conditions and drug release behaviour. Due to the low radio density of soft tissue and vasculature, the application of radio opaque contrast agent is necessary for micro-CT image analysis. The possibility of using different contrast agents for micro-CT imaging is not fully exploited till now and it provides an interesting area of research considering the relevance of micro-CT as a paramount imaging tool.

1.2. Review of Literature

1.2.1. Micro-computed Tomography: Basic Concepts and History

The word tomography is derived from the Greek word "*tomos*" means "section". Tomography is possible with X-rays (X-ray tomography), electrons (electron tomography), visible light (optical tomography), positrons (positron tomography), and acoustic waves (ultrasound tomography) and with the applications of magnetic resonance effect. Thus X-ray tomography is a technique that visualizes the inner structure of samples by virtually slicing the objects by means of X-rays [Clerck and Postnov, 2007].

In conventional radiography, X-rays pass through the investigated object, and the transmitted intensity is recorded as a two-dimensional image. The information contained in this radiograph is a projection of the absorption density in the sample onto the plane perpendicular to the X-ray beam direction. If now the sample is imaged several times in different orientations, three-dimensional (volume) information on the sample structure can be obtained using computer algorithms. This is called a tomographic reconstruction or tomography. It enables one to look at slices of the investigated object without physically slicing it [Luedemann, 2007]. The concept is made use of in clinical computer tomography scanners and a miniaturized version of this is microcomputed tomography.

The first report on micro-CT was published in 1954 [Lindblom, 1954], However, the mathematical basis for the actual CT image reconstruction was presented in two papers by Cormack in 1963 and 1964, respectively [Cormack, 1963 & 1964]. About 10 years later, Hounsfield submitted a patent, describing the first CT scanner, which was then built in 1975 [Hounsfield, 1977]. The possibility of non-invasively imaging three-dimensional sections of a human body was of such importance that Cormack and Hounsfield were awarded with the Nobel Prize for Medicine in 1979 [Cunningham *et al.*, 2003].

As already stated, desktop micro-CT a miniaturized version of medical CT differs from the latter only in two technical aspects. In medical CT X-ray projections are made by rotating the source and detector around the object (patient) resulting in mechanical vibrations where as in micro-CT it is possible to rotate the object, thereby reducing the vibration and enhancing the resolution. The second difference is the size of the X-ray source which is 5-10 μm in micro focus computer tomography compared with millimeters in medical applications. The smaller source increases the sharpness of the projection by reducing the penumbra. This makes it possible to put the object near the X-ray-source and to increase the primary enlargement of the object, which again enhances the resolution [Van Geet, 1997].

Furthermore the micro-CT systems exist with many different modifications. One is based on the use of a synchrotron X-ray source (SμRCT), which is a monochromatic X-ray beam of very small thickness emitted when high energy electrons are accelerated in the magnetic field of a particle accelerator. The other uses a table top X-ray (μCT) source that produces polychromatic radiation but which can be filtered to produce approximately monochromatic radiation [Timothy Hopper, 2005]. Also with the ongoing development of CT systems, this technique became available on many different levels of resolution. Thus, CT is an excellent technique for investigation in a hierarchical fashion ranging from whole bodies down to the sub-cellular level. With the development of micro-CT, complementary techniques as well as new image processing algorithms and analysis techniques have evolved. These new techniques opened the field of micro-CT to many new applications. In spite of the various technical advancements in the system, the physical working principle remains exactly the same [Stauber and Müller, 2008].

1.2.2. Principle

Micro-CT is a variation of X-ray attenuation methods. Attenuation means the graduate diminution of radiation flux through a particular feature due to the process of scattering and absorption of the radiation. In both processes, the X-ray photon

interacts with the atoms of the material. In scattering, the X-ray photon continues with a change in direction with or without a loss in energy. In absorption, the energy of the X-ray photon is completely transferred to the atoms of the material.

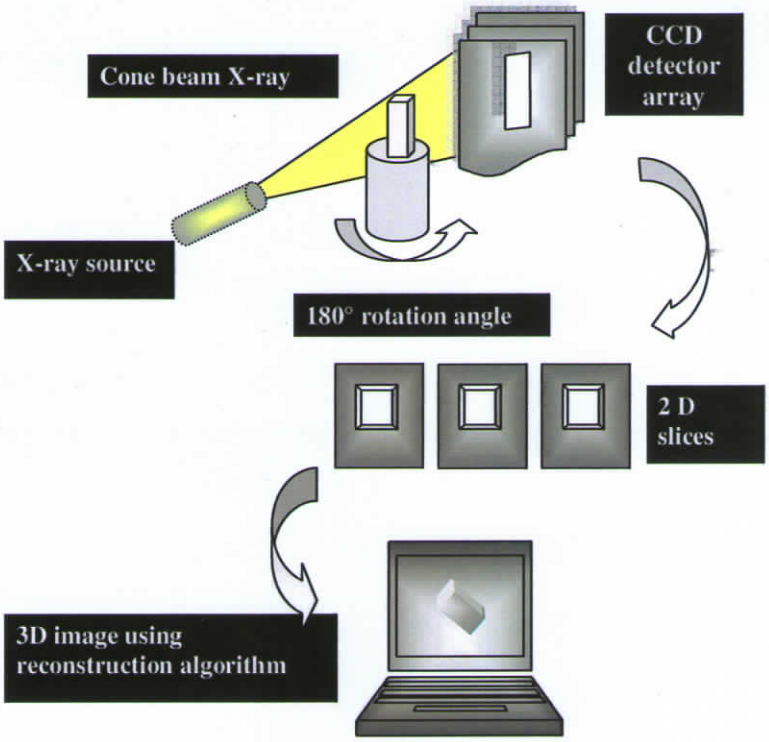

Fig 1: The principle of microcomputed tomography.

The fundamental law of attenuation, also called, Beer-Bouguer-Lambert law, states that the attenuation process is linear to the intensity of radiation and amount of matter, provided that the physical state (i.e., composition) is held constant. The attenuation coefficient is an inherent property, dependent on the atomic number of the object, its density and on the intensity of the X-ray energy, thus allowing quantitative classifications to be made [Davis and Wong, 1996]. Differences in linear attenuation coefficients among tissues are responsible for X-ray image contrast. In computed tomography (CT), the function imaged is in fact the distribution of linear attenuation coefficients [Luedemann, 2007].

The principle of micro-CT involves the reconstruction of the linear attenuation coefficient, within an object, from measurements of the attenuation of an X-ray beam passing through the sample at different viewing angles [Anderson *et al.*, 1996]. Each element of the projection is a line integral of the linear attenuation coefficient in the sample along the X-ray beam path (Salome *et al.*, 1999). A map of the linear attenuation coefficient can then be recovered from these line integrals using suitable reconstruction algorithms [Bonse and Busch, 1996; Kak and Slaney, 1988]. The type of reconstruction algorithm used depends upon the type of X-ray source used.

1.2.3. Components

The simplest common elements of X-ray radiography are an X-ray source, an object to be imaged through which the X-rays pass, and a series of detectors that measure the extent to which the X-ray signal has been attenuated by the object [Ketcham and Carlson, 2001]. Micro-CT is a slight modification of the conventional radiography system. It consists of X-ray beam generated and passed through the object of interest to a scintillator that converts the X-ray to visible light. This light is then passed on to a CCD (usually using fiber optic cables) that converts the light to an electric signal that is then sent to a computer system for data processing [Timothy Hopper, 2005].

In X-ray tubes, X-rays are generated by stopping fast electrons in a target material inside an evacuated glass tube. The energy of the X-ray photons is of the order of the electron energy. The acceleration voltage of electrons determines the upper limit of emitted X-ray energy. X-rays produced by this principle are called Bremsstrahlung with a white continuum spectrum [Bonse and Busch, 1996]. Three variables concern with effectiveness of the X-ray source: focus-size, energy spectrum and intensity. The focus-size is very closely related with the linear resolution of the micro-CT. The energy spectrum is related with the penetrability of an X-ray. Higher energy penetrates more efficiently, but can be less sensitive to changes in material density and composition. The energy spectrum generated is usually described in terms of the peak X-ray energy (kVp). The X-ray intensity directly affects the signal-to-

noise ratio and thus image clarity. Higher intensities improve the underlying counting statistics, but often require a larger focal spot [Ketcham and Carlson, 2001].

After passing through the specimen, the X-rays are detected by a detector system. In micro-CT scanners, a scintillator is often combined with detector. Incident X-ray photon interacts with the scintillator where they are absorbed and light photons are emitted. Light photons enter the fiber optic plate within the scintillator and are carried to the detector. Scintillation screens currently limit the spatial resolution of tomographic systems.

The detector should possess certain characteristics such as: efficiency, spectral sensitivity, linearity, dynamic range and spatial resolution. That is the detector should detect every incident photon of the complete band of X-ray energies, its response should be linear over a large range of intensities and the detector's spatial resolution should match that of the source. Charge-Couple Device (CCD) cameras are mostly applied in micro-CT set up due to its sensitivity to visible light and to prevent damage by the radiation. It will convert the visible light to an electrical signal by means of an Analogue-Digital Converter (ADC) and stored to computer disk memory for further evaluation [Bonse and Busch, 1996]. In detail, CCD is silicon wafer which is an electronic component segmented in to an array of individual light sensitive cells. Each cell is one element of the whole picture formed and is called a 'pixel'. It will detect the X-rays independently and are separated in space.

The raw attenuation data are stored in the computer memory in a floating point matrix. A virtual slice is obtained by applying a reconstruction algorithm and the most accurate one used for micro-CT scanners is *back projection algorithm.* With this algorithm it is sufficient to sum the intensities of all rays that pass through the reconstruction point. The shape of the object is defined by the intercept of the attenuation values that are back projected from the floating-point matrix and converted in to virtual slice. Thus a single virtual cross section is obtained and a series of cross-sections at different vertical levels through the object can be calculated by rotating the specimen about its axis. Decreasing the rotation angle will increase the

number of details that can be seen in the virtual cross sections [Clerk and Postnov, 2007].

1.2.4. Artifacts

The most common artifact in CT imaging is beam hardening. When the mean energy of the exiting photon spectrum is higher than that of the incident spectrum (due to preferential attenuation of the lower energy photons) this will result in an artifact known as beam hardening artifact. This artifact results in streaks in the image between regions of the sample with high attenuation. By adding X-ray filters, the very low energies in the energy spectrum can be removed and as a consequence, the spectrum is narrowed, which reduces beam-hardening artifacts.

Artifacts possibly will ensue from X-ray scatter as a result of the Compton interactions. In these interactions the X-ray beam is deflected from its original course with a random scatter angle, although generally more X-rays are scattered in the forward direction. Artifacts may also crop up due to various other reasons: If the object moves or rotates during the measurement, the projections do not fit together at the reconstruction, resulting in distortion called Motion Artifact. Similarly if the number of projections should not equal at least half the number of samples per projection, the image gets distorted resulting in Aliasing Artifact. Metal Artifacts are caused by materials with a high linear attenuation coefficient leading to total absorption of the X-ray beam causing star-formed artifacts in the reconstructed images. In addition a defect in the scintillator or a defective pixel may develop rings or half-rings around the rotation center of the reconstructed images forming Ring Artifact [Kak and Slaney, 1988; Stauber and Müller, 2008].

1.2.5. Different generations of micro-CT systems

The first generation of micro-CT other wise called point scanning or single detector system is composed of an X-ray source, which emanates parallel geometrical beams, collimator and one single detector. It is the simplest arrangement for the

micro-CT technology. In order to obtain the absorption index map of at least a single cross section of the sample, 1D scanning of the sample or the coupled source-detector unit must be performed [Bonse and Busch, 1996].

The next generation of micro-CT consists of a point source of radiation emanates a fan-shaped beam and, on the other side of the object, a bank of detectors is used to make all the measurements in one fan simultaneously [Kak and Slaney, 1988]. It is also called a linear array system. For 3D examination, it has to be performed a time consuming slice-by-slice examination of the object [Axelsson and Danielsson, 1994].

The cone beam system, which is categorized as the third generation of micro-CT, uses a cone forming source and a 2D detector. Such systems allow complete three-dimensional images to be obtained without the need for scanning each slice individually, so that the complete sample can be radiated at once Also called area-array system, it demands more sophisticated algorithms to reconstruct the image, due to the enhanced polychromatic characteristic of the beams, which leads to beam hardening effects. Nevertheless, the use of sources with small focus size, which diminishes the cone area, leads to less significant errors in reconstruction of the images, when specimen size is small compared to its distance to the X-ray source.

The fourth generation of micro-CT was built to overcome the problems with ring artifacts, common in the cone-beam scanners. This new system employs the method of time delay integration (TDI), which is a technique originally designed for increasing the allowable exposure (or integration) time in the acquisition of linearly moving images. TDI uses a two dimensional CCD which is scanned in such a way, synchronised with the movement of the specimen, so as not to introduce motion blurring [Davis and Elliott, 1997]. Synchrotron radiation sources revolutionized tomographical imaging through high resolution and image quality. The higher flux and continuous spectrum allow researchers to choose a monochromatic beam with a small band pass, which greatly improves the sensitivity of microtomography to smaller X-ray absorption variations within the sample. The high degree of

monochromaticity also mitigates the problem of beam hardening [Cloetens and Baruchel, 2002, Spanne 1989]. However the major limitation with the synchrotron source is the small sample size exposed by the X-ray beam. In addition, availability and access to synchrotron X-ray source is limited [Bentley *et al.*, 2002]. Future developments in micro-CT will include improving the systems with respect to speed, spatial resolution, and new imaging modes. This will broaden the application range of the micro-CT system.

1.2.6. Biomedical Applications

Feldkamp *et al.* were first to build a micro-CT scanner for the evaluation of the three-dimensional micro-structure of trabecular bone. At this stage, micro-CT was an experimental technique available to a few research groups only. However, with the presentation of the first commercially available bone micro-CT scanner in 1994 this technique became quickly a standard in orthopedic research [Feldkamp *et al.*, 1989; Müller and, Rüegsegger, 1994].

Assessment of fracture healing is a common problem in orthopedic practice and research. To determine the effectiveness of certain treatments, drugs, mechanical loads, or rehabilitation regimes, the strength of the fracture callus must be determined. Both clinically and experimentally, there is a need to noninvasively and quantitatively evaluate fracture callus quality during healing. Micro-CT scans were made of the fracture calluses to determine three-dimensional geometry and material properties for the finite element models. Experimentally measured torsional rigidities were compared to finite element solutions. Finite element model predictions of callus rigidity correlated significantly better with experimental torsional rigidity [Shefelbine *et al.*, 2005].

Bone quality includes macro- and micro-architecture, secondary mineralization, bone matrix and micro-damage. CT can be adapted to evaluate both macroscopic and microscopic structure of bone that is orientation, shape and

connectivity of trabeculae can be appreciated and analysed using micro-CT [Qin *et al.*, 2007].

Osteoporosis is a disease characterized by low bone mass and micro-architectural deterioration of bone tissue, resulting in the aggravation of bone fragility and the increase of fracture risk. Bone loss is preferentially at cancellous bone sites. Strong evidences indicate that the loss of bone strength is mainly because of the loss of connectivity of the trabecular bone. Micro computed tomography can be used for trabecular bone evaluation including trabecular thickness, trabecular separation and trabecular number as this may play an important clinical role in early predictions of osteoporosis onset [Zhang *et al.*, 2008].

Not only in orthopedic research, but also in dental research micro-CT has become an effective and nondestructive technique. As reviewed by Swain and Xue [2009], it has been used to measure enamel thickness of a great variety of archaeological specimens and facilitates the study of root canal morphology more precisely. The accuracy of micro-CT in dental research was compared to measurements made by direct measurement, 3D scanner and by photography, the results indicated that micro-CT was a reliable method and might be a useful device for measuring distances and for observing both internal and external tooth structure [Kim *et al.*, 2007]. It can be used for revealing the thickness and area of enamel, dentin, and pulp chamber accurately and reliably. In addition with imaging software, 3D reconstructions could be produced, which also provide volumetric data for enamel and dentin [Gantt *et al.*, 2006]. Although micro-CT is an accurate technique for measuring enamel thickness, however for severely mineralized teeth it may produce a limitation for reliably distinguishing dental tissues. Micro-CT can be used to determine the volume and position of polymeric dental composites in model cavities before and after polymerization. Polymerization shrinkage and potential leakage area can also be determined [Sun *et al.*, 2009].

Micro-CT has been proposed to analyze the scaffold architecture: porosity, surface area per unit volume and degree of pore interconnectivity within scaffolds.

For e.g. calcium phosphate ceramics have been widely investigated in orthopedic tissue engineering and surgery as bone extensors. Micro-CT can provide information regarding the functional pores on the ceramic related implants and characterization of scaffold biomaterials for orthopedic application [Yeung *et al.*, 2007]. Complex ingrowth of bone into the polymer scaffold was also analysed [Jones *et al.*, 2004]. Assessment techniques for scaffold design and their efficacy in bone ingrowth studies require an ability to accurately quantify the 3D structure of the scaffold and an ability to visualize the bone regenerative processes within the scaffold structure. Jones *et al.* [2007] demonstrated the 3-D micro-CT imaging of HAP scaffolds and bone ingrowth in to it. The difference in tissue ingrowth with variation in scaffold architecture was also studied.

Micro-CT has not to date been fully exploited in the area of controlled drug delivery. Controlled drug release devices are designed to release bioactives at a defined rate, over a set time period to achieve therapeutic effects at local or systemic level .The overall rate and pattern of drug release from matrix systems are determined by physico-chemical properties of the drug and polymer, the pore structure of the matrix (pore size, percentage porosity and connectivity) drug diffusion through fluid-filled pores and channels polymer dissolution, erosion or degradation. Micro-CT is used for characterizing the internal 3-D structure of matrix-type drug delivery devices incorporating particulate bioactives. Analysis of micro-CT images can provide detailed quantitative information on macro porosity for correlation with formulation conditions and drug release behaviour [Wang *et al.*, 2009]. The direct relationship between the macro porous structure formed by particle extraction and the original distribution of particulates in the matrix yielded a sensitive quality control measure for evaluating material uniformity and its relationship with formulation conditions.

The major interests of biomedical researchers goes to non–invasive imaging of small live laboratory animals such as rats and mice. The possibility of obtaining 3D information during the life time of an animal opens wide perspectives. One of the first *in vivo* scans was performed on live snails in a conventional *in vitro* micro-CT system; a resolution of 10 μm was achieved. The contribution of micro-CT in

biomedical imaging is limited by the difference in X-ray densities of the particles to be studied [Clerk and Postnov, 2007]. Micro-CT was originally designed to assess the micro and macro architecture of mineralized tissues due to its high radio density. Recently the scope of quantitative micro-CT analysis has grown to include 3D, high resolution imaging and analysis of non-mineralized structures such as soft tissues and vasculature but its low radio density is the major drawback. Thus the application of radio opaque contrast agents will facilitate the 3D micro-CT imaging of soft tissues as well as any objects with low radio density (for e.g. polymer scaffolds, nanofibrous scaffolds etc.) [Lin *et al.*, 2007].

1.2.7. Contrast- enhanced micro-CT imaging

X-ray–based tomographic imaging has been constrained by the low intrinsic X-ray absorption of unmineralized tissue and the lack of established contrast agents [Metscher, 2009a]. As optical densities of soft tissues and water are similar; isolated soft tissues cannot be scanned in saline or any watery solution. Even though the image clarity was low; micro-CT was successfully used in dried lungs, where a distinction is made between tumours and healthy lung tissue due to the increased density within tumours. Calcified inclusions within soft tissues can also be detected. Vascular calcifications due to chronic renal failure in rats are studied using micro-CT [Postnov *et al.*, 2009]. Micro-CT is also used to assess atherosclerosis of the carotid artery in human cadaver samples. The atherosclerotic plaque consisted of soft tissue and calcifications, where the calcifications demonstrated variable internal densities. On the contrary, the density differences within the soft plaque components were less obvious and ulcerations and/or fissures could not be detected. [Mohr *et al.*, 2004]. By using very simple contrast stains micro-CT can be used to make high-contrast, high-resolution, true-3D images of unmineralized tissues.

Immunohistochemistry is commonly used for analysis of soft tissues especially capillaries and arteriole density but this technique failed to provide the 3D vasculature throughout the specimen. Histologic sections can be stacked to render 3D images [Brey *et al.*, 2002], but this approach is subjected to artifacts and require large

processing time. In this regard the radio opaque nature of heavy metal ions is considered and is a better choice to enhance the contrast of low–attenuating materials. Various studies are conducted using heavy metal ions such as barium, lead and iodine as contrast agents. Barium sulfate combined with gelatin has been injected to aid in micro-CT imaging of mouse hind limb vasculature [Duvall *et al.*, 2004]; however clumping of the contrast agent within blood vessels resulted in inhomogeneous distribution of contrast through the micro vasculature.

To visualize renal microvasculature and structures connected to it, an intravascular lead containing polymer, Microfil® (MV-122; Flow Tech, Carver, Mass.), has been favourably used. This approach illustrated the microvascular architecture. A potential limitation of the Microfil vascular perfusion technique is that the analysis must be performed post-mortem. It is also limited to lumen spaces only. Despite limitations these technique is increasingly be used to generate quantitative data regarding the structure of vascular networks in small animal models and also the vessels within other organs of interest, such as the brain and heart of mice and rats [Lin *et al.*, 2007].

Current CT contrast agents are based on small iodinated molecules. Due to its non–toxicity iodine is the most commonly used X-ray contrast agent for *in vivo* and *in vitro* applications. Iodinated contrast agents such as iodixanol and sodium meglumine ioxagalate are used in clinical settings to improve X-ray contrast but the major problem with this is the fast renal clearance. High-resolution micro-CT of low-contrast, small-size vessels in murine models was feasible with liposomal formulations encapsulating high concentrations of iodinated contrast agents, which have long residence times and produce stable, high opacification of the blood pool. But there is the risk of excessive exposure of the subject to free iodine due to iodine leakage from the complex. Thus there is the risk of renal toxicity as well as anaphylaxis in sensitive individuals [Mukundan *et al,* .2006]. Krause *et al.* [2000] observed allergy-like side effects induced by liposome injections in rats and pigs. These were strongly dependant on the size, surface potential and composition of the particles. A human phase I trial was performed with non-PEGylated liposomes of 340

nm, loaded with an iodinated contrast agent to find out its effect on leukocyte count. Leucocytes were depressed for the first 2hrs before showing a rise, particularly pronounced for neutrophilic leucocytes and also a rise in cytokine mediated reactions has occurred [Hallouard *et al.*, 2010].

During *in vitro* micro-CT analysis of immersion fixed or perfusion fixed samples, inorganic iodine stains gave good contrast. Tissues stored in absolute alcohol stained well with iodine. Penetration into tissues was rapid, and contrast imparted to various tissues was excellent, but it has been observed to overstain some mineralized areas resulting in regions of saturation in X-ray images [Metscher, 2009b].

Nevertheless, recent developments indicate that heavy metals, such as osmium tetroxide, may well serve as potential contrast agents in biopsy and post-mortem samples and may increase the versatility of this technique [Gossl *et al.*, 2006]. The K-shell energy of osmium (73.9 keV) and its known tissue binding properties [Kiernan, 1990] make osmium tetroxide a natural candidate for an X-ray contrast stain and also the availability of the stain. Also osmium tetroxide is widely used for studying the scaffold–tissue interaction. Tissue on the scaffolds was stained with osmium tetroxide (OsO_4), following the protocol reported in Seligman *et al.*, to raise the attenuation of the tissue to a level at which both the tissue and scaffold could be detected simultaneously using micro-CT [Hilldore *et al.*,2007]. Micro- CT provides both a 3D image and 3D quantitative analysis of cell spatial distribution within PCL scaffolds after staining the cell seeded scaffold with osmium tetroxide. Scaffolds made from soft natural biomaterial such as collagen do not produce X-ray attenuation for micro-CT. Combination of osmium tetroxide along with other radio opaque stains were used for obtaining a reliable 3Dimage of the scaffold [Farajah *et al.*, 2009]. Osmium is a heavy metal that stains cell membranes and scatters X-rays and makes the cells visible through micro-CT [Shauna *et al.*, 2009]. In spite of all the advantages, its tissue penetration is limited [Hayat, 1970], it does not work well on tissues that have been preserved in alcohol, and osmium is volatile, toxic, and expensive to purchase and to dispose off.

Various stains such as uranyl acetate, lead citrate and phosphotungstic acid used in electron microscopy are capable of imparting radio opacity to low attenuating samples for micro-CT analysis. Uranyl acetate and lead citrate are more often used for the micro-CT analysis of 3D scaffold architecture [Farajah *et al.*, 2009] than for *in vivo* or *in vitro* applications. This limitation may be due to increased toxicity levels compared to other heavy metal stains. Phosphotungstic acid (PTA) is widely used in histology and electron microscopy laboratories and not widely investigated as a contrast agent for micro-CT. PTA was first used for biological staining of structures about 1945. PTA is an anionic stain with a high molecular weight (3313.5 g/mol), which imparts high density to the stained materials generally acting as a negative stain. There is no agreement apparently among biologists as to the interaction of this stain with organic materials, although it is known to stain proteins. Two interpretations regarding the staining mechanism exist: the formation of a complex in aqueous solution and ionic precipitation. In any case, the specificity of staining, at least in biological tissue appears to be related to the pH of the solution , due to the fact that the PTA molecule is unstable and degrades when the pH is higher than 1.5 [Linda *et al.*, 2008].

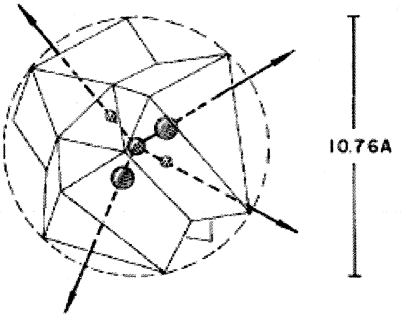

Fig 2: Schematic representation of phosphotungstic acid. [In the tribasic phosphotungstate anion, each of the four polyhedra represents the W_3O_{10} group and they are arranged tetrahedrally around the central phosphorus atom (Ladoulis and Gill, 1970)].

According to Metscher (2009b) PTA staining produces excellent contrast among different tissues. The staining is stable for at least several months but penetration is much slower than iodine since PTA is a much larger molecule and hence the time duration required for staining is comparatively more. For e.g. chick embryos later than approximately stage 24 required overnight or longer incubation times for better stain penetration. PTA is known to bind heavily to various proteins and connective tissue and this property, along with electron-shell energies that match common X-ray source emissions, suggested that it might be a useful stain for X-ray imaging.

In view of the importance of nanoscience in each and every field of biomedical technology, nanoparticle-based contrast agents are becoming ever more valuable mostly in biomedical imaging. Nanomaterials have become progressively more important in the development of new molecular probes for in *vivo* micro-CT imaging, both experimentally and clinically. Rabin *et al.* [2006] demonstrated the utility of polymer-coated Bi_2S_3 nanoparticles for enhanced in *vivo* imaging of the vasculature, the liver and lymph nodes in mice. This was found to have excellent stability, high X-ray absorption and long circulation time compared to iodine. Among the various nanoparticles studied so far, gold nanoparticles are particularly well suited to biological applications due to their photo-stability, water solubility and non-toxicity [Kumar *et al.*, 2008]. Gold nanoparticles (GNPs) have been used widely in imaging and therapeutics due to their surface plasmonic properties. Recently, GNPs are also demonstrated to have great potential as contrast agents for computed tomography (CT) imaging applications. According to Hainfeld *et al.*, [2006] gold nanoparticles absorb more X-rays than the heavy metal contrast agents such as iodine (3 x at 100 keV), enabling higher contrast at lower X-ray dose and higher resolution.

Nondestructive 3D imaging techniques such as micro-CT are increasingly providing a powerful set of quantitative tools to aid the development and evaluation of porous biomaterials and new approaches to engineering tissues and organs [Guldberg *et al.*, 2008]. In this aspect, contrast enhancers are indispensable agents which can provide adequate contrast to inherently radiolucent synthetic and natural

polymers which are widely employed in vascular tissue engineering. Furthermore, *in situ* quantitative imaging can reduce the cost and improve the efficiency of *in vitro* experiments.

Although the application of heavy metals in the different fixation and staining steps is well known in the preparation of samples for conventional transmission electron microscopy studies, their use in the preparation of biological tissue for X-ray micro-CT investigation has not yet been completely developed. At the same time various novel contrast agents based on nanoparticles are being developed and proved to improve the attenuation better than the conventional contrast agents. These comparative studies are usually carried out *in vivo*. But for the *in vitro* micro-CT analysis of various biological samples and scaffolds the nanoparticles are not widely applied and their attenuation efficiency is not weighed against the conventional ones. Hence these contrast agents is of relevance in this regard and will provide a necessary tool for the imaging of low attenuating materials in particular polymer tissue construct.

1.3. Hypothesis

The development of an *in situ* imaging methodology for monitoring *in vitro* cellular proliferation in polymer scaffolds can provide valuable insight onto the progression of tissue regeneration especially for vascular tissue engineering applications. Synthetic as well as natural polymer scaffolds and their tissue constructs used in vascular tissue engineering applications are inherently radio-translucent in nature which denies the opportunity to employ advanced radiographic imaging tools. Development of suitable staining agents may aid to overcome this limitation by enhancing the overall contrast of these polymer scaffolds and/or tissue constructs. Hence an attempt to develop suitable staining agents which can visualize and quantify the micro-architectural characteristics of polymer scaffolds as well as polymer-tissue constructs might be able to provide valuable contributions to the imaging aspects of vascular tissue engineering.

1.4. Objectives

As per the strategy discussed above, two metal-based contrast agents were selected, viz; Phosphotungstic acid (PTA) and Gold nanoparticle (GNP) based on their merits with respect to vascular tissue engineering applications. Following are the major aims of the present study:

- Synthesis and development of comparatively non-toxic, cost-effective metal-based contrast agents possessing micro and/or nano particulate structure.

- Optimization, characterization and comparative study of these agents to evaluate their efficacy in imaging polymer scaffolds and polymer-tissue constructs.

- Development of X-ray based high definition imaging methodology using microcomputed tomography for *in situ* three-dimensional visualization of polymer-tissue constructs in dynamic and static culture mode.

Materials and Methods

Chapter II

Materials and Methods

2.1. Materials and Instrumentation

The chemicals and equipments used in the study are listed in Tables 2.1.1 and 2.1.2 respectively.

Table 2.1.1: Chemicals used in the study

No	Name of the chemical	Grade	Source
1	Phosphotungstic acid hydrate	R & D	Sigma Aldrich, USA
2	Polycaprolactone (M.W. 42,500)	R & D	Sigma Aldrich, USA
3	Gold (III) chloride trihydrate	A.C.S.	Sigma Aldrich, USA
4	Sodium citrate trihydrate	A.C.S	Sigma Aldrich, USA
5	Iscove's modified Dulbecco's Minimal Essential medium	Cell culture grade	Invitrogen, USA
6	Paraformaldehyde	LR	SD Fine-Chem Ltd., India
7	Sodium bicarbonate	Cell culture Grade	Sigma Aldrich, USA
8	Antibiotic-antimycotic solution	Cell culture grade	Invitrogen, USA
9	Foetal bovine serum	Cell culture grade	Invitrogen, USA
10	Trypsin-EDTA	Cell culture grade	Invitrogen, USA
11	Sodium hydroxide	AR	SD-fine-Chem Ltd., India
12	Maygrunwald stain	Cell culture grade	Sigma Aldrich, USA
13	Giemsa stain	Cell culture grade	Sigma Aldrich, USA
14	Hydrochloric acid (35.4%)	AR	SD-Fine-Chem Ltd., India
15	Sodium chloride	Extrapure	SD-Fine-Chem Ltd., India
16	Potassium dihydrogen phosphate	GR	MERCK, Germany
17	Disodium hydrogen phosphate	GR	MERCK, Germany

Table 2.1.2: Equipments used in the study

No	Name of the equipment	Model	Make
1	Micro Computed Tomography	μCT-40	Scanco Medical AG, Switzerland
2	Particle Size Analyzer	ZEN3600	MALVERN, Canada
3	Transmission Electron Microscope	H-7650	Hitachi, USA
4	UV-VIS Spectrophotometer	HP- 8453	Hewlett Packard, USA
5	Fluorescence spectrophotometer	Cary Eclipse	VARIAN, USA
6	Refractometer	NAR-3T	ATAGO, Japan
7	Ultra sound sonicator	Bandelin UC-60W	ICW, India
8	Ultra centrifuge	Optima ™-L-90K	Beckmann Coultier, USA
9	Refrigerated Centrifuge	Contifuge Stratos	Heraeus, UK
10	Deep freezer	Forma 900 series	Thermo Scientific, USA
11	Lyophilizer	Alpha 1-4 LD	CHRIST, Germany
12	Flash Rotavaporizer	RV 06-ML	IKA, Germany
13	Perfusion pump	MINIPULS® 3	Gilson, Netherlands
14	Carbondioxide incubator	Thermo	Thermo electron Ltd., USA
15	Light Microscope	DM IRB	Leica, Germany
16	Environmental Scanning Electron Microscope-EDAX	Quanta™ 200	FEI, Netherlands
17	Ion sputter	E-1010	Hitachi, USA

2.1.3. Specifications of Micro-CT

The details of the Micro-CT system (Fig: 3) used in the present study are listed below:

Table 2.1.3.1: Features of Micro-CT system used in the present study

Particulars	**µCT 40**
Type	Fully shielded Desktop cone-beam micro-CT
X-ray source	30 - 90 kVp / 20 - 50 keV (160 µA)
Detector	2048 x 256 elements, 24 µm pitch
Resolution	6 - 72 µm nominal isotropic (pixel size)
Image matrix	512 x 512 to 4096 x 4096 pix
Max. scan size	36.9 x 80 mm (ØxL)
Max. specimen size	36.9 x 80 mm (ØxL)
Electrical	100 - 230 V / 50 - 60 Hz, 345 W
Dimensions	810 x 1100 x 420 mm (HxWxD)
Sample holder	1. PMMA(Poly-Methyl-Methacrylate)tubes 2. PEI (Poly-Ether- Imide) tubes

The system is provided with comprehensive softwares for scanning, 3D analysis, visualization, image management and data import/export. The scan program provides a clear, powerful interface for managing scanning parameters, which include X-ray beam energy and intensity, resolution, measurement time and desired density calibration. Parameter settings can be written to database as control files for repeated use in large projects, ensuring that results can be compared reliably, and settings used in previous measurements can be viewed and reused.

Reconstruction of 3D data sets from micro-CT projection data, including beam-hardening correction, is handled automatically after completion of each cone-beam image stack. Tomographic image reconstruction is an inherently parallel

operation. Standard acquisition and reconstruction protocols handle very large numbers of projections, with small angular separation, to deliver images with high signal-to-noise ratio and high resolution.

Scan data are viewed in the evaluation program in XY, XZ, YZ and 3D MPR (Multi-Planar Reformatting) representations. Material density can be viewed in several units including mg HA/ccm or Hounsfield, and density profiles can be inspected interactively. In addition, distances between features can be measured in both 2D and 3D.

Regions- and volumes-of-interest (ROI or VOI) are easily and flexibly defined by drawing contours in slices, with morphing interpolating contours between slices semi-automatically. Evaluation of 3D scan data is handled by IPL (Image Processing Language), an advanced script-based 3D-volume analysis tool.

Fig 3: X-ray microcomputed tomography instrument (Scanco μCT 40)

2.2. Methods

2.2.1. Micro-CT imaging of Phosphotungstic acid (PTA)

Phosphotungstic acid hydrate powder was packed in a X-ray translucent material and aligned vertically in the sample holder (PMMA tube) for detecting the X-ray attenuation with imaging parameters set at 45keV, 6µm slice thickness and 177 µA.

2.2.2. Staining of Polycaprolactone (PCL) scaffold using PTA

Polycaprolactone scaffolds (PCL, M.W. 42,500) of 8 cm length x 4mm inner diameter and wall thickness 0.025mm to 0.05mm were prepared in the laboratory and used for the present study. Scaffolds were sectioned to pieces of 1cm length and incubated in different concentrations of the stain (0.1%, 0.3%, 0.5%, and 0.7%) for 16 hours and 0.9% and 1% for 4hrs. After incubation, the scaffolds were washed thoroughly with absolute alcohol and air dried for 15 min. Micro-CT imaging of the scaffolds were performed with the parameters set as mentioned above. The µCT evaluation version 6.0 software system was used for 2D image generation and threshold input [set at a range of 30- 135 (1/1000)]. The attenuation histograms of the scaffolds stained with different concentrations of PTA stain were plotted and the compared to that of the unstained scaffold.

2.2.3. Synthesis of gold nanoparticle (GNP)

GNP was synthesized based on the protocol standardized by Kumar *et al.* (2008) 1 ml of 12.7 mM chloroauric acid solution (Appendix I) is added to 49 ml of DI Water (Thermo Scientific Barnstead DIamond™ TII Water Systems,USA) in a clean 100-ml glass beaker containing a stirrer bar. The entire apparatus was placed on a magnetic stirrer cum hot plate (Schott, Germany) and heated to boiling while stirring at 370 rpm. 0.94 ml of 38.8 mM trisodium citrate solution (Appendix I) was added drop wise into the reaction mixture at a temperature of 98° C. Upon the addition of trisodium citrate, the color of the solution changed to blue in 30s and then to red in another 150s. After the formation of red colour the solution was boiled for another 5 mins and cooled to room temperature (RT) while stirring. It was then transferred to screw cap vials and stored at room temperature.

$AuCl_3 + 2e^- \longrightarrow AuCl + 2Cl^-$

$3AuCl \longrightarrow 2Au^o + AuCl_3$

The overall reaction is:

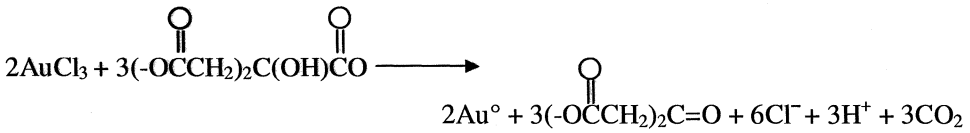

$$2AuCl_3 + 3(\text{-OCCH}_2)_2\text{C(OH)CO} \longrightarrow 2Au^\circ + 3(\text{-OCCH}_2)_2\text{C=O} + 6Cl^- + 3H^+ + 3CO_2$$

2.2.4. Characterization of GNP

2.2.4.1. Particle size analysis

Gold nanoparticle solution was filtered (0.22µm GHP membrane filter) and sonicated for 10 mins. The refractive index of the solution was measured using refractometer to determine the size distribution. Particle size analysis was carried out using a dynamic light scattering (DLS) instrument.

2.2.4.2. UV- VIS Spectroscopy

The absorbance of the aqueous solution gold nanoparticle (filtered and sonicated) was measured using UV-VIS spectrophotometer (HP Chemstation Software) at a wave length range of λ= 515-530 nm.

2.2.4.3. Transmission electron microscopy

Liquid suspension of GNP was kept on a copper grid and air dried. The copper grid was then viewed under TEM with an acceleration voltage set at 60kV at a resolution of 200 nm with a magnification of x15.0 k.

2.2.4.4. Fluorescent spectroscopy

Aqueous solution of gold nnanoparticle was taken in a quartz cuvette and the fluorescence emission spectra at different excitations (450nm, 480 nm, 500 nm and 530 nm) were recorded using a fluorescent spectrophotometer (Cary Eclipse Software).

2.2.4.5. Micro-CT imaging of GNP

50 ml of the gold nanoparticle solution was ultra centrifuged at 13,000 rpm, 10° C for 45 min, thrice. Pellet was collected and resuspended in 1 ml of the supernatant, deep freezed at -80 °C overnight and then lyophilized. The gold nanopowder thus obtained was analyzed using micro-CT with the same imaging parameters mentioned in section 2.2.2 and the attenuation histogram was constructed.

2.2.5. Staining of PCL scaffolds with GNP

PCL scaffolds (1 cm x 4mm ID) were incubated in GNP solution for 24 hrs. Micro-CT imaging of the scaffolds were performed with the same imaging parameters (Sec: 2.2.1) and imaging software (Sec: 2.2.2) as already mentioned.

2.2.6. Cell culture studies

Human umbilical vein endothelial cells (HUVECs) were isolated as per the standard protocol [Jaffe *et al.*, 1973]. The HUVECs were cultured in Iscove's Modified Dulbecco's Minimal essential medium (IMDM) supplemented with 20% foetal bovine serum, sodium bicarbonate (1 mg/ml) and antibiotic-antimycotic solution (1x). After 80% confluency is reached, the cells were trypsinised (Trypsin-EDTA- 0.05 %) and centrifuged. The cell pellet was resuspended in 1 ml of the medium.the cells were counted using heamocytometer.

Scaffolds used for the present study were PCL scaffolds (Sec: 2.2.2) sterilized by immersing in 70% alcohol overnight. The cells after trypsinization were resuspended in the medium and seeded onto the scaffolds at a density of $5x10^5$ cells/cm^2.

Two types of culture methods were followed: Static (cell seeded scaffolds were immersed in the medium) and Perfusion mode (medium is perfused through the scaffolds using a perfusion pump).The cell seeded scaffolds were kept in a CO_2 incubator. Medium was changed once in two days and the culture was maintained for 8 days.

2.2.7. Fixation and staining of the cell seeded scaffolds

GNP solution was added on to the dynamic and static cultures (half the number of scaffolds), at the end of 8^{th} day in the ratio 2: 1 and incubated for 24hrs. The cell seeded scaffolds with and without GNP were washed twice in PBS and fixed in 1% parafomaldehyde overnight.

After overnight fixation the scaffolds were washed twice with PBS. A portion of the scaffolds without GNP were stained with phosphotungstic acid (0.3%) overnight.

2.2.7.1.. Light microscopic examination

The fixed scaffolds were stained with MayGrunwald-Giemsa (MGG) stain. The scaffolds were incubated for 1 hr in MGG stain and washed thoroughly with distilled water. The cell morphology on the scaffolds were analysed by light microscopical examination (magnification X10, X20 and the imaging software is Leica Application Suite V3).

2.2.7.2. Micro-CT imaging of cell seeded scaffolds

Cell seeded scaffolds treated with GNP as well as PTA were used for Micro-CT examination. The scaffolds were washed thoroughly with PBS and air dried. Micro-CT examination was done with same parameters as mentioned previously (Sec. 2.2.2 and 2.2.3) and the threshold was set at 0.28 (1/cm).

2.2.7.3. Environmental Scanning Electron microscopy-Energy Dispersive X-ray Absorptiometry

The cell seeded scaffolds were kept in 3% gluteraldehyde fixative overnight. Then washed twice in phosphate buffer (pH 7.4) and dehydrated using ascending grades of alcohols and mounted on an aluminium stub. The EDAX spectra were recorded at an acceleration voltage of 20 kV. After taking the EDAX the samples were coated with gold using an ion sputter and images were taken at X3000 magnification with the same acceleration voltage.

Result and Discussion

Chapter III

Results and Discussion

3.1. Micro-CT imaging of PTA

The radiograph of PTA powder shown in Figure 4a is found to exhibit intensive brightness and the consecutive reconstructed 2D cross-sectional images obtained after X-ray imaging is shown in figure 4b.

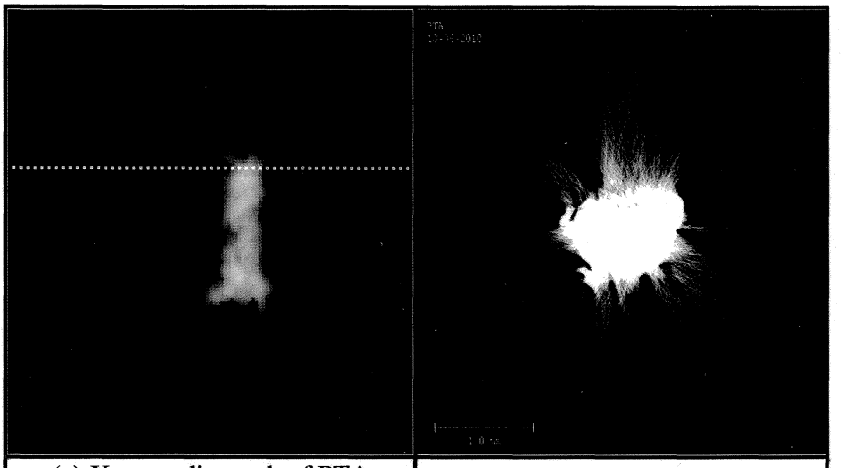

(a) X-ray radiograph of PTA powder	(b) 2D image of PTA powder

Fig 4: Micro-CT images of PTA powder

3.2. Contrast enhancement of PCL scaffold with PTA

2D cross-sectional images of PCL scaffolds stained with varying concentrations of PTA exhibits considerable change in their attenuation with respect to each other (Figure 5a, 5b & 5c). PCL scaffolds were exposed to different concentrations of PTA stain (0.1, 0.3, 0.5 and 0.7%) for 16 hours and 0.9 and 1% only for 4 hours especially because 16hr exposure of the scaffolds in these concentrations of the stain tended to make it highly fragile and unable to image whereas scaffolds in other concentrations were found to remain intact. The brittleness of scaffolds at higher concentrations of stain may be attributed to the accelerated hydrolysis of polymer at

Chapter III

Results and Discussion

3.1. Micro-CT imaging of PTA

The radiograph of PTA powder shown in Figure 4a is found to exhibit intensive brightness and the consecutive reconstructed 2D cross-sectional images obtained after X-ray imaging is shown in figure 4b.

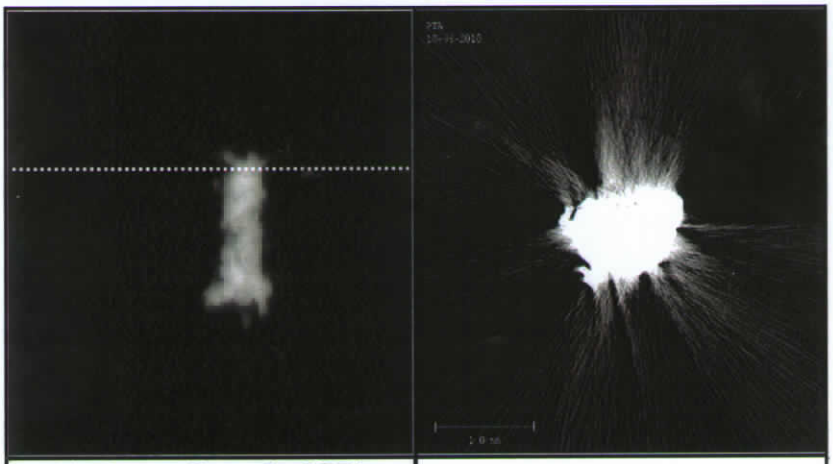

(a) X-ray radiograph of PTA powder	(b) 2D image of PTA powder

Fig 4: Micro-CT images of PTA powder

3.2. Contrast enhancement of PCL scaffold with PTA

2D cross-sectional images of PCL scaffolds stained with varying concentrations of PTA exhibits considerable change in their attenuation with respect to each other (Figure 5a, 5b & 5c). PCL scaffolds were exposed to different concentrations of PTA stain (0.1, 0.3, 0.5 and 0.7%) for 16 hours and 0.9 and 1% only for 4 hours especially because 16hr exposure of the scaffolds in these concentrations of the stain tended to make it highly fragile and unable to image whereas scaffolds in other concentrations were found to remain intact. The brittleness of scaffolds at higher concentrations of stain may be attributed to the accelerated hydrolysis of polymer at

lower pH. Maximum attenuation was found to be for scaffolds stained with 1 % PTA solution exposed for 4 hours (Figure 5c).

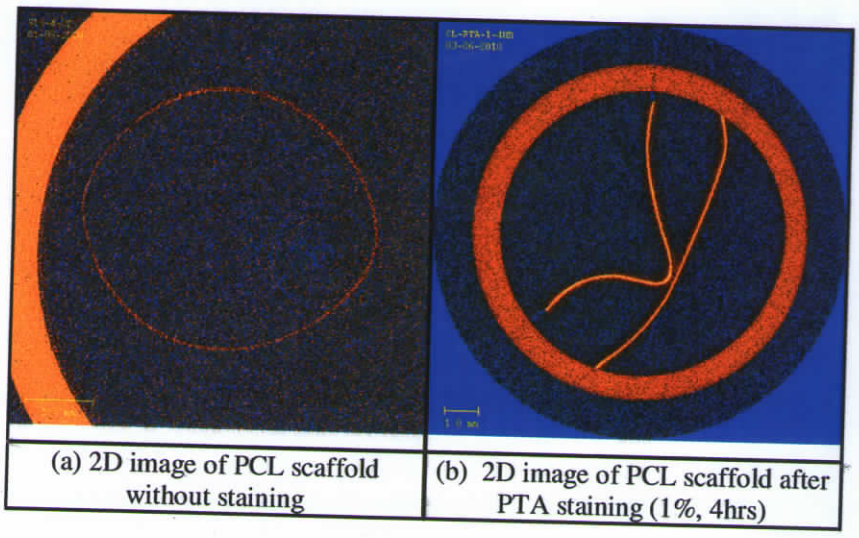

(a) 2D image of PCL scaffold without staining

(b) 2D image of PCL scaffold after PTA staining (1%, 4hrs)

Fig 5: 2D cross-sectional images of PCL scaffold before and after staining

Figure 6 shows the X-ray attenuation histogram of bare PCL scaffold with respect to stained PCL scaffolds. The unstained PCL scaffold possesses lowest voxel intensity range whereas the scaffold stained with 1% PTA for 4 hrs attains highest voxel intensity. With the increase in stain concentration, the voxel intensity ranges also shifts towards higher magnitude. Hence it may be concluded that PTA has sufficient affinity towards scaffolding material which in turn has resulted in the higher attenuation at higher concentrations. The affinity may be because of the fact that PTA can react with surface functional groups such as hydroxyl and/or carboxyl as a positive stain which are present in PCL scaffolds [Linda *et al.*, 2008].

lower pH. Maximum attenuation was found to be for scaffolds stained with 1 % PTA solution exposed for 4 hours (Figure 5c).

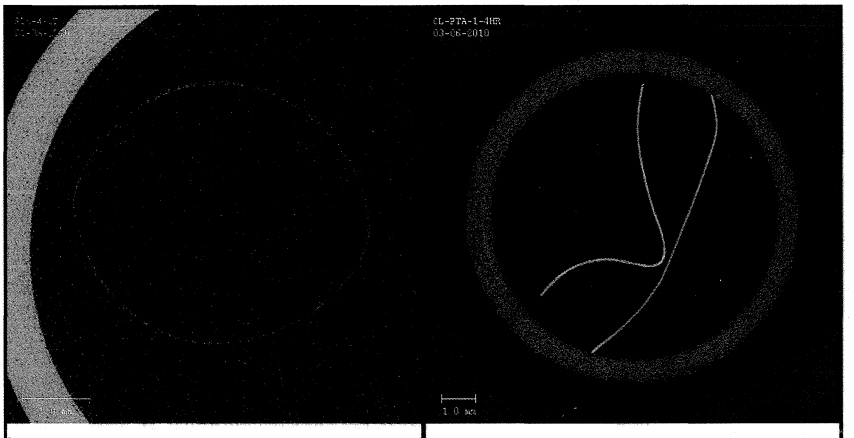

(a) 2D image of PCL scaffold without staining	(b) 2D image of PCL scaffold after PTA staining (1%, 4hrs)

Fig 5: 2D cross-sectional images of PCL scaffold before and after staining

Figure 6 shows the X-ray attenuation histogram of bare PCL scaffold with respect to stained PCL scaffolds. The unstained PCL scaffold possesses lowest voxel intensity range whereas the scaffold stained with 1% PTA for 4 hrs attains highest voxel intensity. With the increase in stain concentration, the voxel intensity ranges also shifts towards higher magnitude. Hence it may be concluded that PTA has sufficient affinity towards scaffolding material which in turn has resulted in the higher attenuation at higher concentrations. The affinity may be because of the fact that PTA can react with surface functional groups such as hydroxyl and/or carboxyl as a positive stain which are present in PCL scaffolds [Linda *et al.*, 2008].

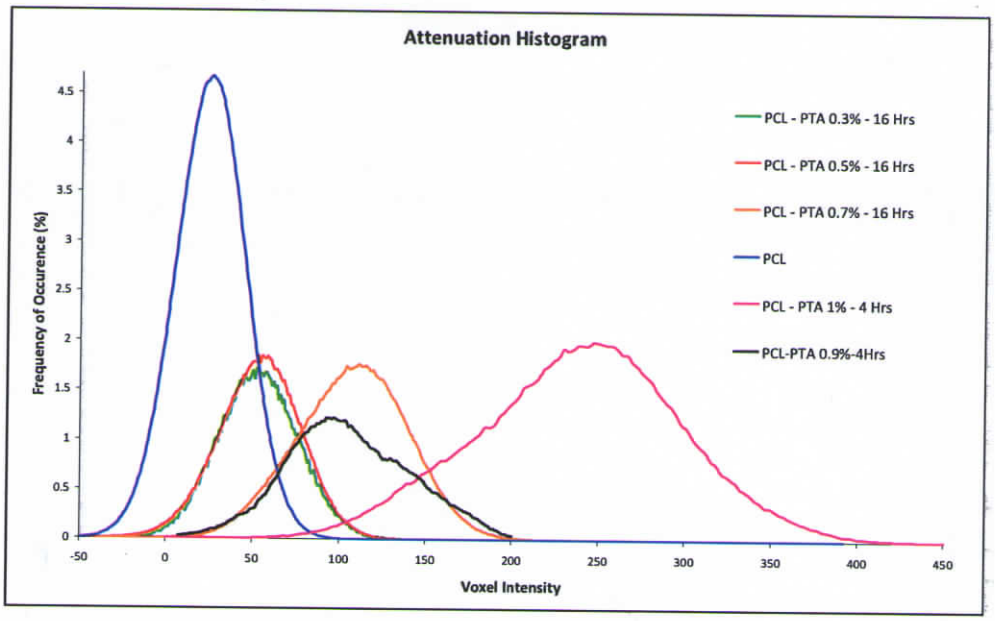

Fig 6: X-ray attenuation histogram of unstained and stained PCL scaffolds

3.3. Synthesis and characterization of gold nanoparticle:

Gold nanoparticles in aqueous dispersion (Fig: 7) is prepared by trisodium citrate reduction using $HAuCl_4$. The size and shape of the gold nanoparticle synthesized are characterized using TEM and DLS. The TEM images (Fig: 8) of the gold nanoparticle showed particles within a size range of 15- 20 nm and are spherical in shape. A plot of size distribution by intensity and volume are obtained through DL S measurement and the particle size range is approximately 20-30 nm (Figs: 9&10). The particle size measured by DLS is higher than that obtained by TEM. This is because DLS generally measures hydrodynamic diameter, it provides a basically different measure of particle size than electron microscope, which determines electron diffraction.

In general larger particles scatter light much more efficiently than smaller particles. Therefore, even small traces of agglomerates or dust in a sample can interfere with the DLS measurement. It also measures the equivalent-sphere

hydrodynamic diameter and provides no information about particle shape. Thus a measure of the overall size distribution of the particles in the solution will show an increase [Hall *et al.*, 2007]. In the present study so as to avoid uncertainties associated with any one measurement techniques, multiple systems are used for the characterization of the synthesized nanoparticles.

Fig 7: Aqueous solution of GNP

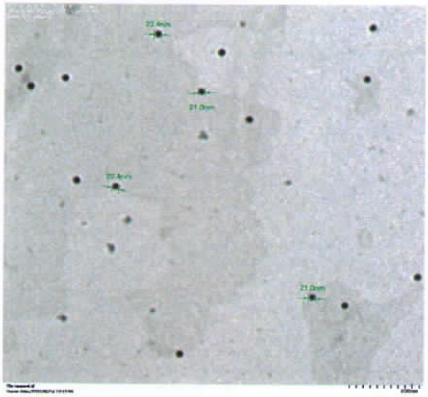

Fig 8: TEM image of GNP
(Magnification: x15000)

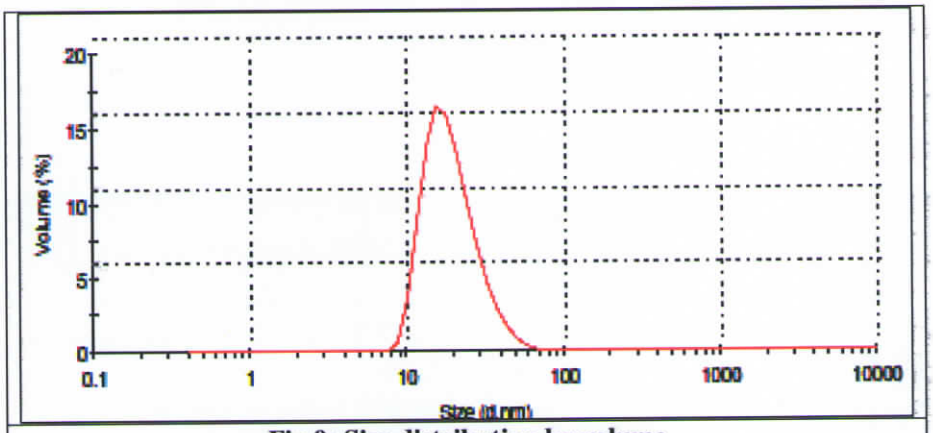

Fig 9: Size distribution by volume

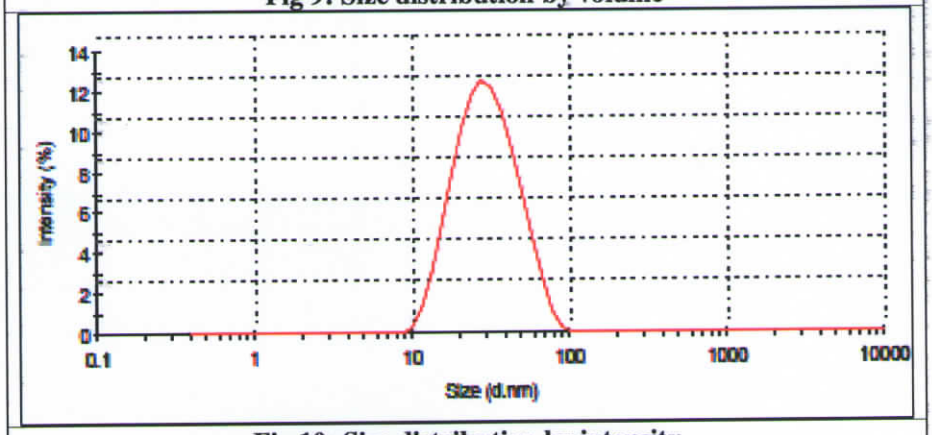

Fig 10: Size distribution by intensity

The relationship between the size of the nanoparticle and the UV absorbance is depicted in many studies. As the particle sizes increase, the absorption spectra show a gradual red-shift in the plasmon resonance absorption peak [He *et al.*, 2008]. The UV absorbance spectrum of gold nanoparticle synthesized in this study is found to be 524 nm (Fig: 11). Gold nanoparticles with diameters between 12-20 nm are known to effectively scatter visible light in the wave length region around 530 nm [Eck *et al.*, 2008]. Previous studies have shown that broadening of the spectrum indicate aggregation of particles (Kumar *et al.*, 2008), but in this case spectrum exhibits a better peak shape. This indicates that the particles are around 20 nm in size and are stable in aqueous solutions at room temperature.

According to He et al. [2008] the fluorescence emission of GNPs will not vary with size and is constant around an emission wave length of 610 nm (at an excitation of 532 nm), but the emission spectra indicate that the fluorescence emission intensity at 610 nm is prominent in particles of larger size (55 nm) and is negligible incase of particles of smaller size. In the present study fluorescent emission of GNPs (20 nm) at different excitation wave lengths is recorded and the maximum fluorescence emission intensity is found to be at 532 nm when the excitation wavelength is around 450 nm (Fig: 12).

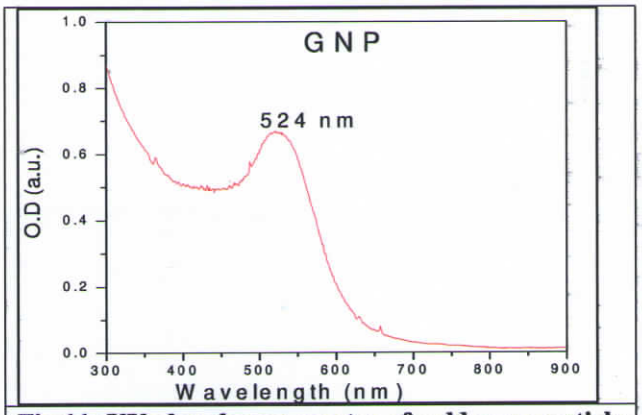

Fig 11: UV absorbance spectra of gold nanoparticle

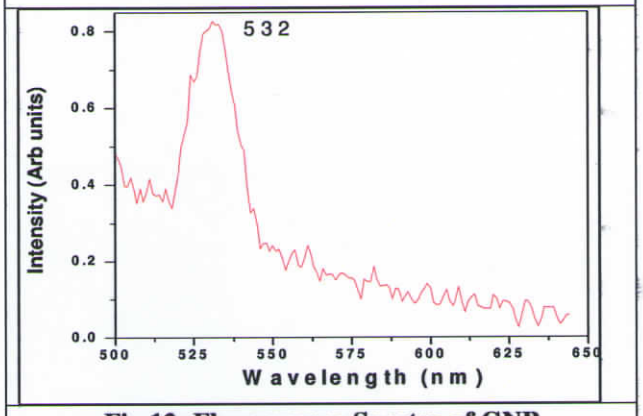

Fig 12: Fluorescence Spectra of GNP

The fluorescence property of gold nanoparticle often depends on various surface modifications. The fluorescence intensity of the naked GNP is relatively

fainter than those with surface modifications. Generally, fluorescence of solid Au(I) compound is stronger than that of samples in solution, because Au(I)-Au(I) bands may break in solution, and leads the fluorescence disappear [Zhang *et al.*, 2007]. The GNPs synthesized in the current study is without any surface modification and also it is an aqueous monodisperse solution. Therefore *the fluorescent property of gold nnanoparticle is not reliable in this case as detection method.*

The relevance of GNP in the present study is to confirm its ability as a contrast agent for micro-CT. In micro-CT imaging, smaller GNPs (of less than 10 nm size) are more preferred due to their X-ray attenuation than larger ones. Studies by Xu *et al.* [2008] states that increased X-ray attenuation of small sized GNPs may be due to the larger surface area and thus they serve as excellent CT contrast agents. But the major drawback with these small sized nanoparticles is their poor cellular uptake [Levy *et al.*, 2010] and cytotoxicity [Pan *et al.*, 2007]. The size and shape dependent effect of gold nanoparticle on cellur uptake is studied by Chitrani *et al.* [2006] and they found out that 50 nm size, spherical gold nanoaprticles show maximum cellular uptake and the small sized nanoaprticles are not readily endocytosed by the cells. Thus *smaller the size of the nanoparticle, the better will be the X-ray attenuation, but for imaging of living cells it is not well suited.*

The radiograph of GNP powder shown in figure 13a exhibits intensive brightness and the consecutive reconstructed 2D cross-sectional images obtained after X-ray imaging were shown in figure 13b. As stated above the histogram indicates a linear attenuation coefficient similar to that of PTA (7.997 cm^{-1}) (fig. 14). There are several reports of improved attenuation of GNP than conventional contrast agents. Xu *et al.*, compared the X-ray attenuation of GNPs at different concentrations with a commercial iodinated-contrast agent, Omnipaque. But they found out that even though the theoretical attenuation of gold is higher (at 100 keV: gold, 5.16 cm^2/g; iodine, 1.94 cm^2/g; water, 0.171 cm^2/g), practically there is not much difference in attenuation between both in aqueous solution.

In aqueous solution or dispersion, the attenuation of the samples will exhibit comparatively low attenuation than that of air as the imaging medium. This is because the optical density of water is higher than that of air. Consequently it will offer more attenuation to X-rays and thus the attenuation of materials in aqueous solution will be less noticeable. That is why in the present study both *the contrast agents in their solid state are used to determine their highest X-ray attenuation coefficient.*

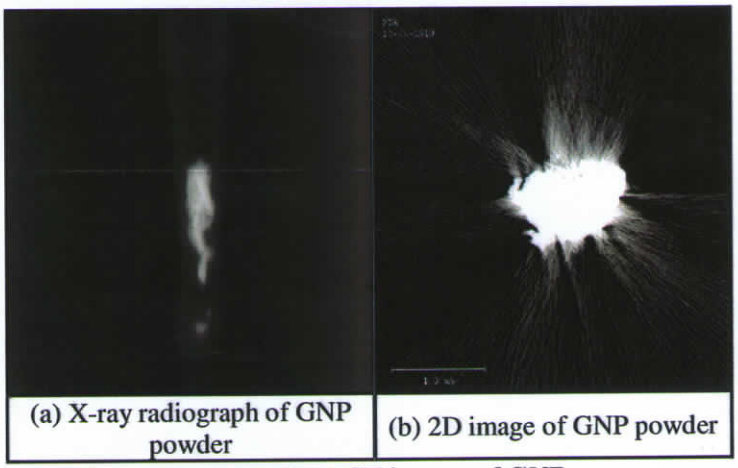

(a) X-ray radiograph of GNP powder | (b) 2D image of GNP powder

Fig 13: Micro-CT images of GNP

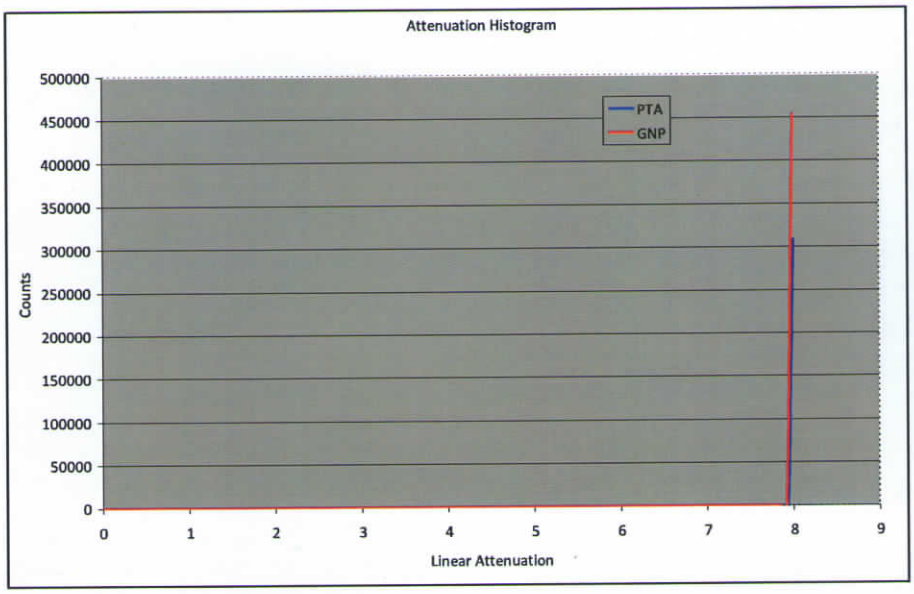

Fig 14: X-ray attenuation profile of PTA and GNP powder

The attenuation profile of PTA and GNP (Fig: 14) indicates the competence level of both as excellent contrast enhancers for micro-CT. Even though PTA is used in electron microscopy, its X-ray attenuation property is not fully utilized till now, where as GNP is a well established nanoscale X-ray contrast agent proved to be of higher attenuation than conventional ones. In the present case *the heavy metal stain PTA exhibits excellent X-ray contrast comparable to GNP.*

3.4. Contrast enhanced imaging of the PCL scaffold with GNP

PCL scaffold is incubated in GNP solution for 24 hrs and the micro-CT image is shown in Fig: 15a where there is not much variation in attenuation compared to the control sample (Fig: 5). A comparison between the attenuation histogram of the PTA stained PCL scaffold and GNP stained one give a clear idea that PTA is most suited to stain low attenuating polymer scaffolds (Fig: 15b). PTA can improve the attenuation of the polymer by reacting with surface functional groups; on the contrary GNPs have no affinity towards the polymer; however the chance of improving the affinity through surface modifications cannot be neglected.

(a) 2D micro-CT image of GNP stained PCL scaffold

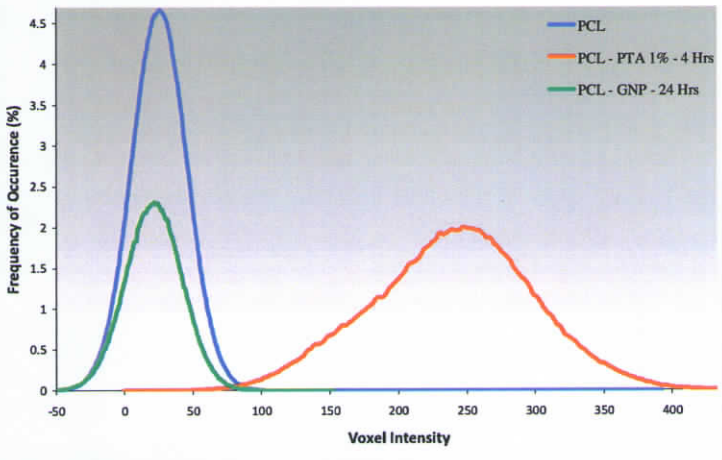

(b) Voxel intensity histogram of PCL scaffold stained with GNP and PTA

Fig 15: 2D image and voxel intensity histogram of GNP stained PCL scaffold

3.5. Micro-CT imaging of cell seeded scaffold *via* contrast enhancement

3.5.1. Contrast enhancement through PTA

For imaging cells using micro-CT difference in the magnitude of contrast enhancement between control specimen and cell seeded polymer scaffold has to be quantified [Dorsey *et al.*, 2009]. To measure the difference in magnitude of contrast enhancement, voxel intensity histogram of specimens were plotted against their total voxel volume contribution, as shown in Fig. 16. From the histogram an optimal threshold value is depicted, from the voxel intensity axis which represents a non-zero value for stained specimen containing cells whereas a zero value for control specimen.

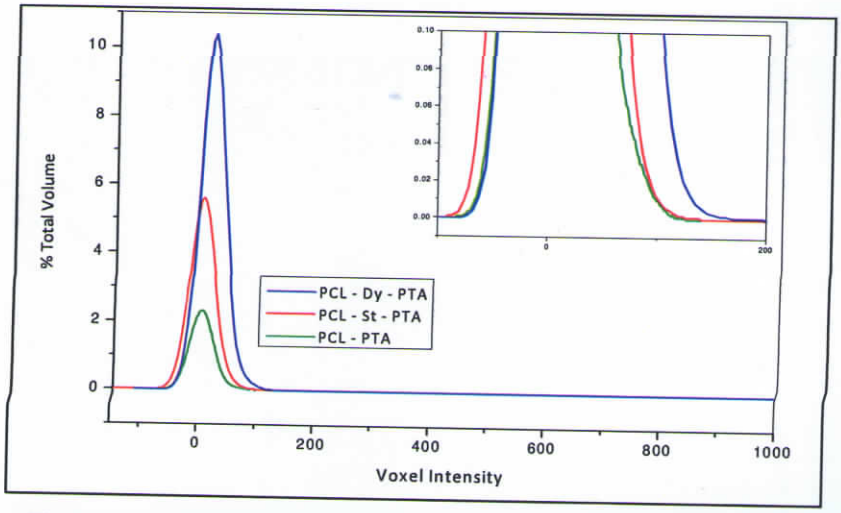

Fig 16: Voxel intensity histogram of PTA stained cell seeded PCL scaffolds in dynamic and static mode

The threshold value selected thereafter is employed for reconstruction of the 2D images onto 3D images visualizing overall cell distribution in PCL scaffolds (Fig: 17c & 17d). The 2D micro-CT images of the cell seeded scaffolds after contrast enhancement using PTA is given in Figure 17a & 17b. The attenuation histograms of the cell seeded PTA stained PCL scaffolds (PCL-dynamic and PCL-static) were compared to that of the bare PCL scaffold stained with PTA (0.3%, 16 hrs) [Metscher,

2009b]. The PCL scaffold cultured in dynamic mode exhibited maximum attenuation compared to those in static mode and the optimum threshold was 127.

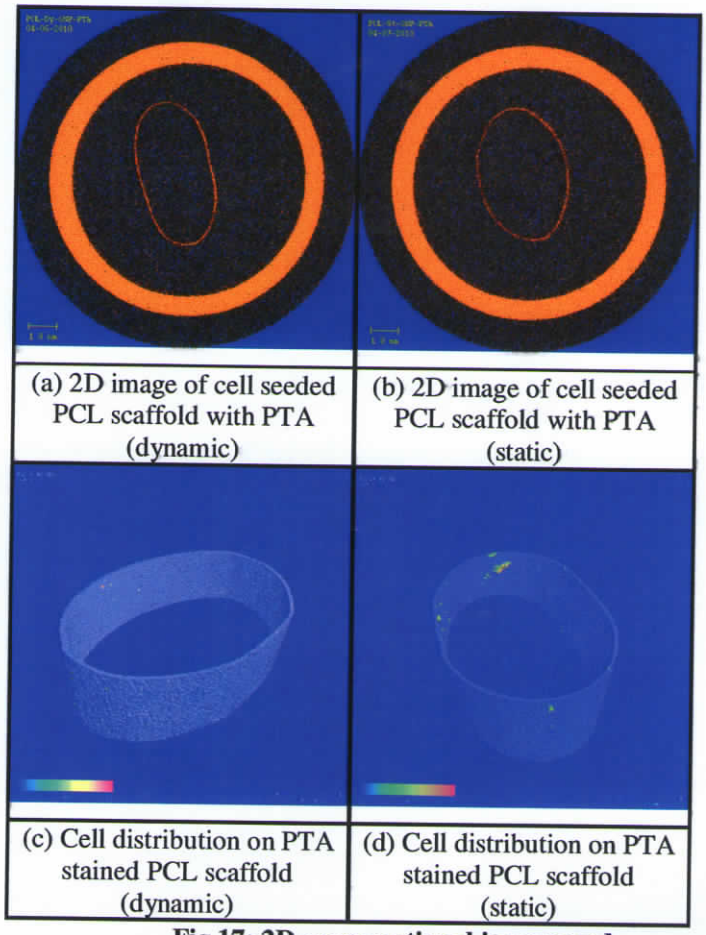

(a) 2D image of cell seeded PCL scaffold with PTA (dynamic)

(b) 2D image of cell seeded PCL scaffold with PTA (static)

(c) Cell distribution on PTA stained PCL scaffold (dynamic)

(d) Cell distribution on PTA stained PCL scaffold (static)

Fig 17: 2D cross-sectional images and 3D images of cell seeded PCL scaffolds

The cell tissue volume in both the scaffolds was quantified using the same threshold. Cell tissue volume distribution and the cumulative cell volume in dynamic culture is more than that in static culture as shown in Figure 18 and 19. This is because the dynamic culture exhibits improved cell growth and specific cell distribution due to the effect of hemodynamic forces during medium perfusion mimicking its natural environment. Previous studies indicate that the proper fluid

2009b]. The PCL scaffold cultured in dynamic mode exhibited maximum attenuation compared to those in static mode and the optimum threshold was 127.

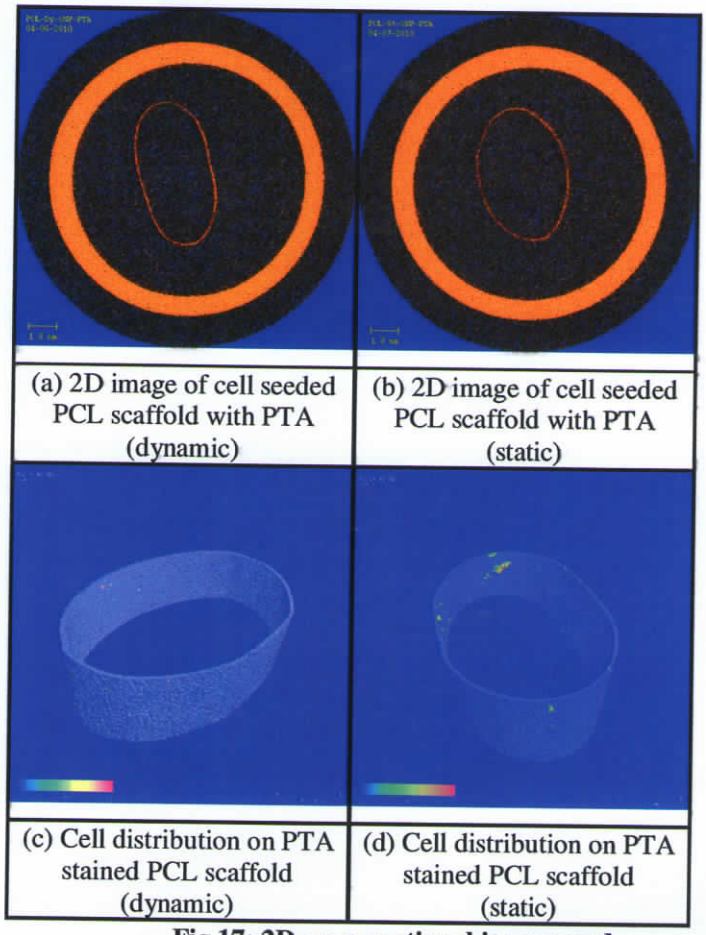

(a) 2D image of cell seeded PCL scaffold with PTA (dynamic)

(b) 2D image of cell seeded PCL scaffold with PTA (static)

(c) Cell distribution on PTA stained PCL scaffold (dynamic)

(d) Cell distribution on PTA stained PCL scaffold (static)

Fig 17: 2D cross-sectional images and 3D images of cell seeded PCL scaffolds

The cell tissue volume in both the scaffolds was quantified using the same threshold. Cell tissue volume distribution and the cumulative cell volume in dynamic culture is more than that in static culture as shown in Figure 18 and 19. This is because the dynamic culture exhibits improved cell growth and specific cell distribution due to the effect of hemodynamic forces during medium perfusion mimicking its natural environment. Previous studies indicate that the proper fluid

dynamic forces resulting from the medium flux through the surface of the cell layer keeps the cells in a high proliferative state [Kaiser *et al.*, 1999].

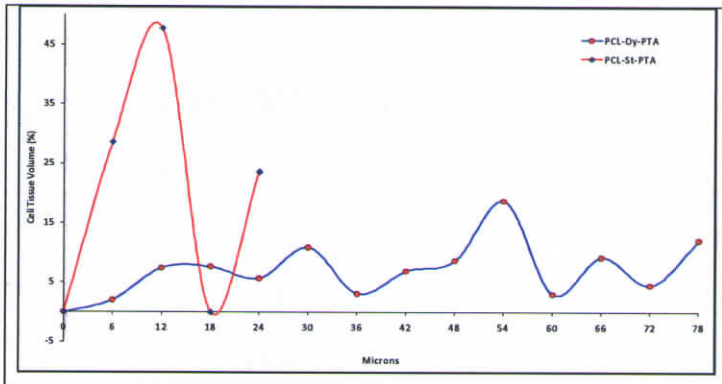

Fig 18: Cell tissue volume distribution

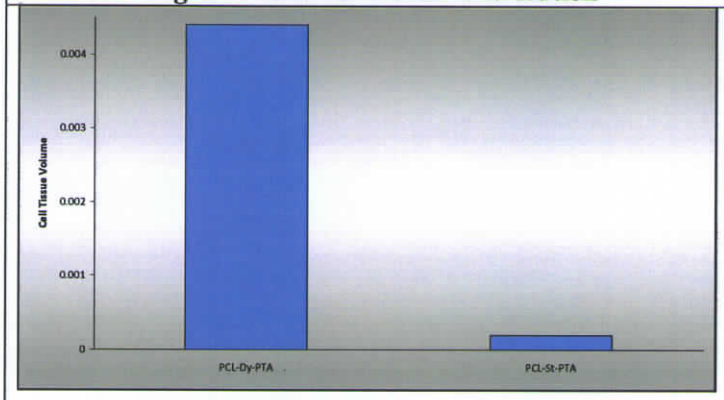

Fig 19: Cumulative cell volume

3.5.2. Contrast enhancement through GNP

The protocol employed for imaging cell volume using PTA is deployed thereafter for imaging cell volume of GNP stained PCL scaffolds. The optimal threshold value obtained from the voxel intensity histogram of GNP stained PCL scaffolds is 102 as shown in Figure 20. Thereafter the 3D images of cell distribution and 2D images of GNP stained scaffold is given in Figure 21. The cell volume distribution as well as cumulative cell volume in PCL scaffolds stained with GNP also shows the same pattern (Figs: 22 and 23). However there is a significant reduction in the cumulative cell volume observed in GNP stained specimens compared to PTA stained specimens which may be attributed either due to reduced uptake of GNP by the cells or due to resolution limit of the instrument (6 microns).

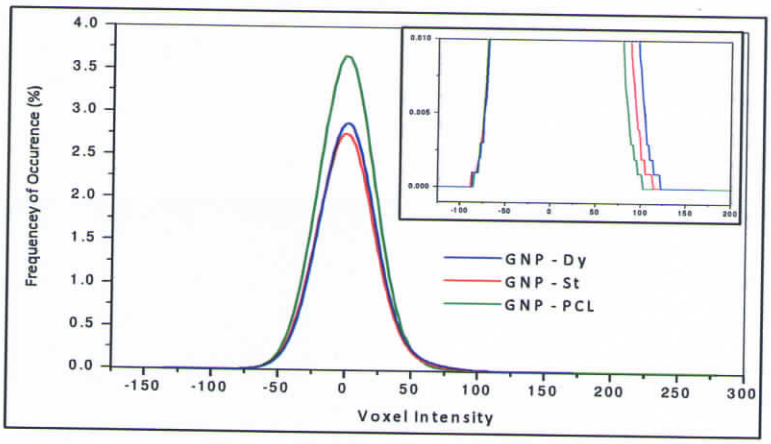

Fig 20: Voxel intensity histogram of GNP stained PCL scaffolds - dynamic & static

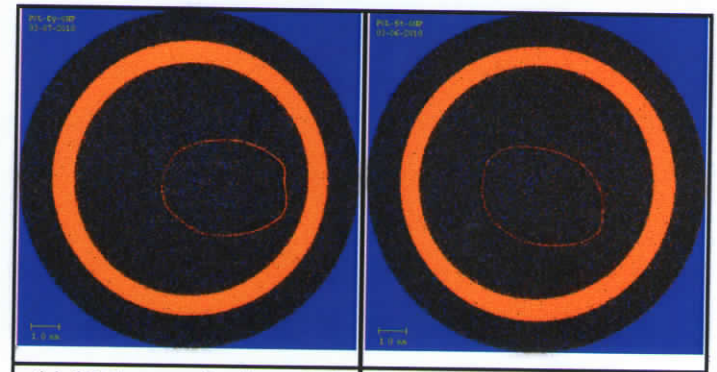

(a) 2D image of cell seeded PCL scaffold with GNP (dynamic)

(b) 2D image of cell seeded PCL scaffold with GNP (static)

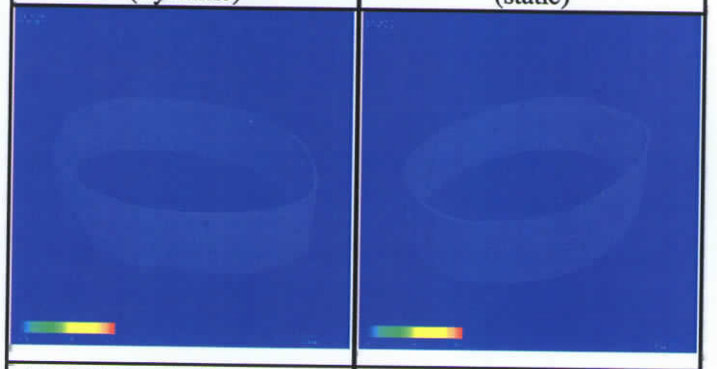

(c) Cell distribution on GNP stained PCL scaffold (dynamic)

(d) Cell distribution on GNP stained PCL scaffold (static)

Fig 21: 2D images GNP stained cell seeded PCL scaffold

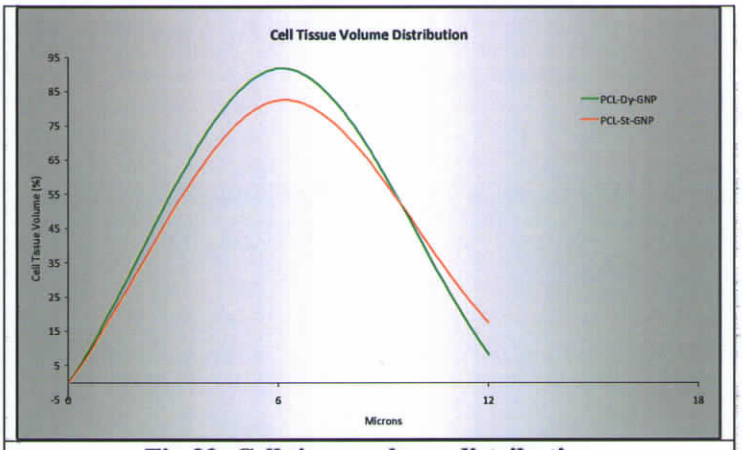

Fig 22: Cell tissue volume distribution

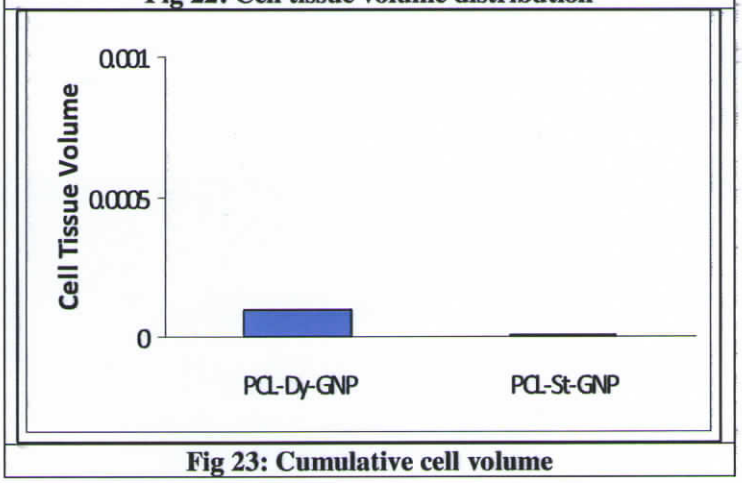

Fig 23: Cumulative cell volume

3.6. Light microscopic examination

Light microscopic examination of MGG stained scaffolds revealed the cellular morphology and cell coverage (Fig: 24). The cell morphology on the scaffold lumen showed cobblestone nature typical of endothelial cells. Under dynamic culture conditions the cells exhibited elongated morphology. This is due to the medium flow through the lumen.

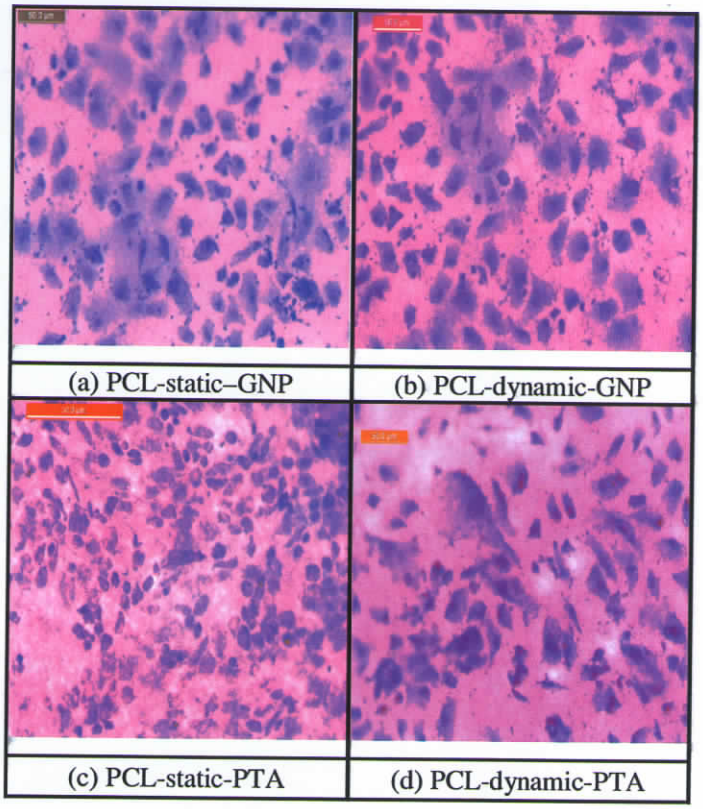

Fig 24: Light microscopic images (X20) of GNP and PTA stained cell seeded PCL scaffolds

3.7. SEM –EDAX studies of cell (HUVECs) seeded scaffolds

As discussed earlier, the attenuation histograms of cell seeded scaffolds indicate an increase in attenuation as compared to the control. The affinity of PTA to PCL polymer is already proved (Sec: 3.2). But gold nanoparticles have poor affinity towards the polymer scaffolds as such (Sec: 3.4). Thus the increase in attenuation after GNP addition may be due to the uptake of the nanoparticle by the HUVECs seeded on to the PCL scaffolds. In order to confirm the presence of gold nanoparticle, the EDAX spectra of the cell seeded scaffolds (Fig: 25) were taken.

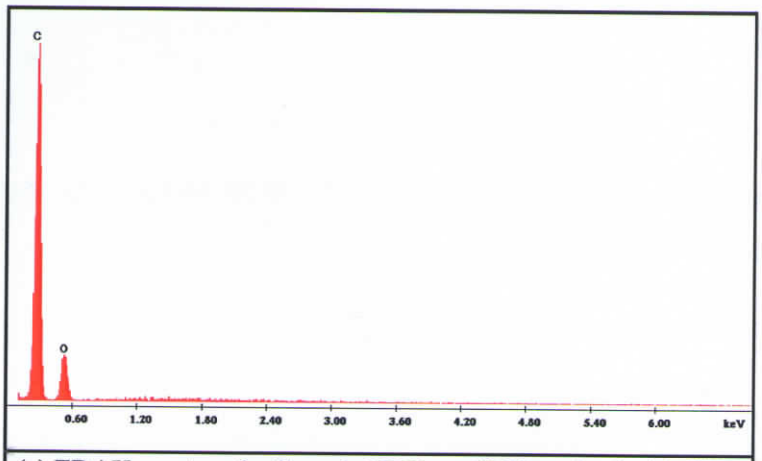

(a) EDAX spectra of cell seeded PCL scaffolds stained with GNP (dynamic)

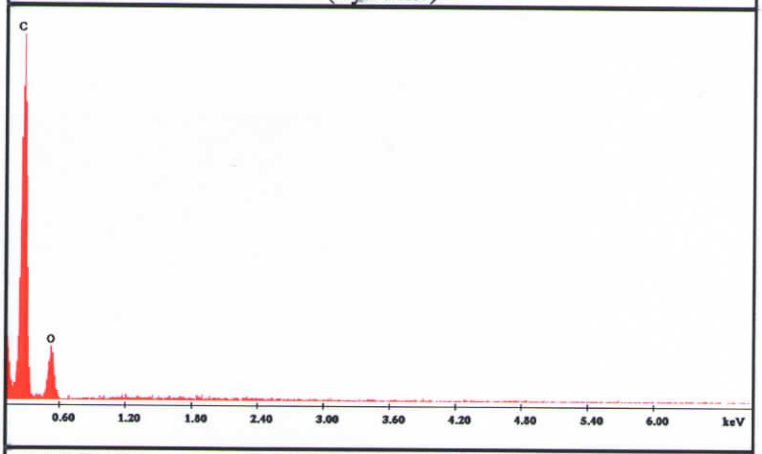

(b) EDAX spectra of cell seeded scaffolds PCL scaffolds stained with GNP (static)

Fig 25: EDAX spectra of GNP stained cell seeded PCL scaffolds

The EDAX spectrum is unable to present any noticeable peaks of gold nanoparticle. In the spectrum, the prominent peaks indicate the presence of carbon and oxygen, because the living cells as well as the polymer scaffolds contain both these elements in higher quantities. Thus these spectrum peaks may be masking the presence of GNP which is comparatively present in low concentrations. In addition another possible reason is that GNP may be internalized by the cells through non receptor mediated endocytosis. Through EDAX, the bulk elemental composition can only be analyzed, thus the internalized nanoparticles are unable to detect.

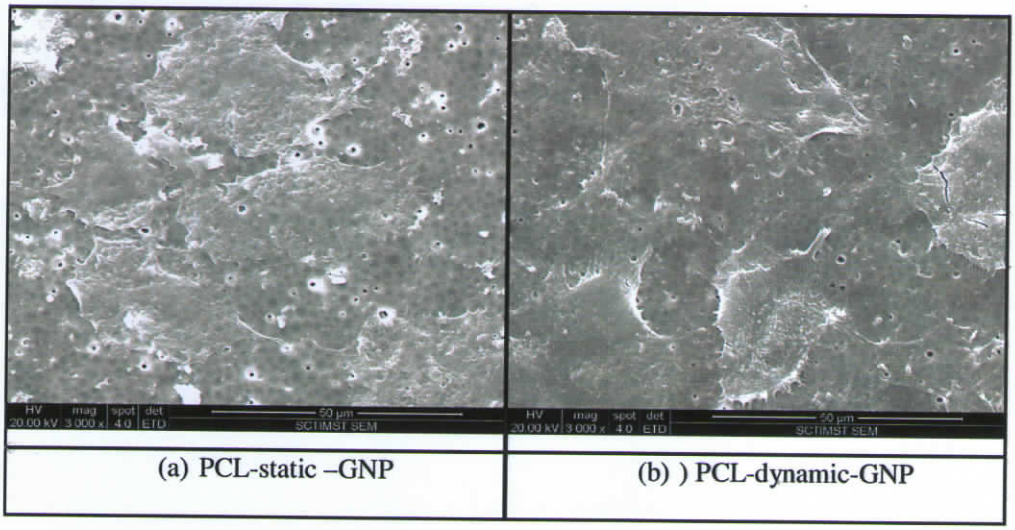

(a) PCL-static –GNP

(b)) PCL-dynamic-GNP

Fig 26: SEM pictures of GNP stained PCL scaffolds in dynamic and static mode

The scanning electron micrographs (Fig: 26) of the cell seeded scaffolds clearly showed the attachment of cells and also the morphology of the cells. As the sample is a cell seeded polymer scaffold, it is not easy to visualize through any alternate methods such as TEM because of practical limitations in sample preparations. Furthermore the polymer itself is having fluorescence because of which the fluorescence imaging cannot provide any information on the presence of GNP.

Chapter IV
Summary and Conclusion

4.1. Summary of the current study

In the present work, the X-ray attenuation of PTA powder was determined using micro-CT exhibiting a high linear attenuation coefficient (7.997 cm^{-1}). Similarly Gold nanoparticles were synthesized and characterized using different techniques such as TEM, DLS, UV-VIS absorbance spectrum and fluorescent spectrum. The linear attenuation coefficient of GNP determined using micro-CT showed same value as that of PTA (7.997 cm^{-1}). The characterization studies indicates that synthesized GNP possess a particle size around 20 nm, which is appropriate for imaging of live cells as well as for producing enough X-ray attenuation. If the particles are of larger size (above 50 nm) then the X-ray attenuation property seems to reduce and if particles are of smaller size (less than 10 nm) then the cellular uptake will be poor and will have to address the problem of cytotoxicity. Thus the optimal particle size used in this study is standardized as 20 nm.

The next stage of this study includes the application of these contrast agents on to low attenuating polymer scaffold such as PCL. Application of different concentrations of the alcoholic PTA solutions for different time periods to these scaffolds resulted in marked difference in attenuation which can be clearly visualized from the 2D cross sectional images of micro-CT. An examination of the attenuation histograms of these scaffolds were plotted against the bare PCL scaffolds showed that the optimum stain concentration that can produce highest attenuation was found to be 1 % within an exposure time of 4 hours. However PCL scaffolds incubated in GNP solution for 24 hrs did not show much variation in attenuation profile compared to the PTA stained one. It is concluded that this may be due to the reactivity of PTA to the surface functional groups of the polymer where as GNP is lacking any reactivity with the polymer.

Observations with cell seeded PCL scaffolds cultured in dynamic and static mode after seeding with HUVECs, stained with MGG and examined using light microscopy revealed that the cell morphology and cells exhibited a cobblestone arrangement and uniform growth throughout the scaffold. Subsequently the cell seeded scaffolds were imaged using micro-CT by staining with PTA (0.3 %, 16 hrs) and GNP (24 hrs) and a plot of cell volume and cell distribution was obtained. PTA stained scaffolds presented better information regarding the cell volume and distribution than GNP stained ones. *Both PTA and GNP stained scaffolds indicates that cell volume and distribution was significant in dynamic culture mode rather than in static culture mode.* This was substantiated by the fact that during dynamic culture the fluid dynamic forces stimulate the cells to high proliferative state. Further investigation of the GNP stained scaffolds were performed with ESEM-EDAX to analyze the growth pattern of cells on the scaffolds though it could not conclusively confirm the presence of GNP either due to its low concentrations or the prominent spectrum peaks of carbon and oxygen where as the scanning electron micrographs presented cell growth pattern similar to that of the light microscopic images.

4.2. Conclusions

In brief the present study is mainly aimed at the development of an appropriate contrast enhancement method for soft biological materials and low attenuating polmers in order to facilitate their 3D visualization using micro-CT. The main observations of the present study are concluded as follows:

- PTA and GNP powder possess higher X-ray attenuation coefficient of 7.997 cm^{-1}.
- PTA (1% for 4 hours) is most suited for improving the attenuation of the polymer scaffolds than GNP.
- Gold nanoparticles having a particle size of ~ 20 nm could be successfully synthesized and characterized in the laboratory which showed a UV-VIS absorbance of 524 nm and maximum fluorescence emission intensity at 532 nm.
- The light microscopic examination of the HUVECs seeded on to PCL scaffolds clearly visualizes the cell morphology.

- The SEM pictures also provide information regarding the cell morphology and cell growth pattern on the scaffolds. The EDAX spectra recorded prominent peaks of carbon and oxygen while presence GNP is not confirmed.
- PTA stained cell seeded scaffolds exhibits significant cell volume and distribution than GNP stained scaffolds. In both PTA and GNP stained scaffolds, cultured in dynamic mode show prominent cell volume and distribution compared to static.

4.3. Future Prospects

PTA meets the requirements of a radiographic contrasting agent and can be further employed for micro-CT imaging of both synthetic as well as natural scaffolds to study their micro-architectural characteristics. Since PTA posses sufficient affinity towards ECM components it can be further utilized for *in vitro* imaging of biological specimens which lacks inherent X-ray attenuation. Even though GNP is unable to enhance the contrast of cell seeded polymer scaffolds in the same magnitude as that of PTA, surface functionalization and/or directional bio-conjugation can equip them to enhance the contrast by increased adsorption and/or affinity towards polymer-tissue constructs. Development of such a strategy can pave the way towards *in situ* 3D imaging of polymer-tissue constructs especially in the arena of vascular tissue engineering.

References

References

1. Amanda Hilldore, Abigail Wojtowicz, AmyWagoner Johnson. Micro-CT based quantification of non-mineralized tissue on cultured hydroxyapatite scaffolds. J Biomed Mater Res. 2007; 82A: 1012–1021.

2. Anderson P, Elliott J C, Bose U, Jones S J. A comparison of the mineral content of enamel and dentine in human premolars and enamel pearls measured by X-ray microtomography. Arch Oral Biol. 1996; 41(3): 281-290.

3. Andreas Mohr, Ruediger Wenke, Frank W Roemer, John A Lynch, Christian Gatzka, Markus Priebe, Ali Guermazi, Mikayel Grigorian, Martin Heller, Stefan Mueller-Huelsbeck. Micro-CT of Carotid Arteries: A Tool for Experimental Studies. Cardiovasc Intervent Radiol. 2004; 27: 651–654.

4. Angela S P Lin, Ashley W Parmer, Craig L Duvall, Galen C Robertson, Megan E Oest, Bina Rai, Marc E Levenston, Robert E Guldberg. Contrast-Enhanced Micro-CT imaging of Soft tissues. In. Ling Qin, Harry K Genant, James F Griffith and Kwok -Sui Leung (eds). Advanced Bioimaging Technologies in Assessment of the Quality of Bone and Scaffold Materials: Techniques and Applications. New York: Springer; 2007: 417-429.

5. A A Postnov, P C D Haese, E Neven, N M De Clerck, V P Persy. Possibilities and limits of X-ray microtomography for *in vivo* and *ex vivo* detection of vascular calcifications. Int J Cardiovasc Imaging. 2009; 25: 615–624.

6. Anthony C Jones, Bruce Milthorpe, Holger Averdunka, Ajay Limaye, Tim J Senden, Arthur Sakellariou, Adrian P Sheppard, Rob M Sok, Mark A Knackstedt, Arthur Brandwood, Dennis Rohner, Dietmar W Hutmacher. Analysis of 3D bone ingrowth into polymer scaffolds via micro-computed tomography imaging. Biomaterials. 2004; 25: 4947–4954.

7. Anthony C Jones, Christoph H Arns, Adrian P Sheppard, Dietmar W Hutmacher, Bruce K. Milthorpe, Mark A. Knackstedt. Assessment of bone ingrowth into porous biomaterials using Micro CT. Biomaterials. 2007; 28: 2491–2504.

8. Armen R Kherlopian, Ting Song, Qi Duan, Mathew A Neimark, Ming J Po, John K Gohagan, Andrew F Laine. A review of imaging techniques for systems biology. BMC Syst Biol. 2008; 2: 74.

9. Axelsson C, Danielsson P. Three-dimensional reconstruction from cone-beam data in O (N3logN) time. Phys Med Biol. 1994; 39: 477-491.

10. Bonse U, Busch F. X-ray computed microtomography (μCT) using synchrotron radiation (SR). Prog Biophys Mol Bio. 1996; 65(1-2): 133-169.

11. Brey E M, King T W, Johnston C, McIntire L V, Reece G P, Patrick C W. A technique for quantitative three dimensional analysis of micro vasculature structure. Micro vasc res. 2002; 63(3): 279-294.

12. Brian D Metscher. Micro-CT for comparative morphology: simple staining methods allow high-contrast 3D imaging of diverse non-mineralized animal tissues. BMC Physiology. 2009; 9a: 11.

13. Brian D. Metscher. Micro-CT for Developmental Biology: A Versatile Tool for High-Contrast 3D Imaging at Histological Resolutions. Developmental dynamics. 2009b; 238: 632–640.

14. Charles T Ladoulis, Thomas J Gill. Physical chemical studies on the Specific interaction of an Acriflavine-phosphotungstic acid complex with double-stranded nucleic acids. Jour. of cell biol. 1970; 47: 500-511.

15. Chenjie Xu, Glenn A. Tung, and Shouheng Sun. Size and Concentration Effect of Gold Nanoparticles on X-ray Attenuation As Measured on Computed Tomography. Chem Mater. 2008; 20(13): 4167–4169.

16. Cloetens P, Baruchel J. Synchrotron-radiation Microtomography. European SynchrotronRadiationFacility.2002.Available: http://www.esrf.fr/UsersAndScience/Publications/Highlights/2002/Imaging/IMA1/Daculs

17. Cormack A M. Representation of a function by its line integrals with some radiological applications. J. Appl. Phys. 1963; 34: 2722–2727.

18. Cormack A M. Representation of a function by its line integrals with some radiological applications. II. J. Appl. Phys. 1964; 35: 2908–2913.

19. Davis G R, Wong F S L. X-ray microtomography of bones and teeth. Physiol Meas. 1996; 17(3): 121-146.

20. Davis G R, Elliott J C. X-ray microtomography scanner using time-delay integration for elimination of ring artefacts in the reconstructed image. Nucl Instr and Meth in Phys Res A. 1997; 394(1-2): 157-162.

21. Devika Chithrani B, Arezou A Ghazani, Warren C W Chan. Determining the Size and Shape Dependence of Gold Nanoparticle Uptake into Mammalian Cells. Nano Lett. 2006; 6*(4)*: 662–668.

22. Dirk Kaiser, Mark A. Freyberg, Gangolf Schrimpf, Peter Friedl. Apoptosis Induced by Lack of Hemodynamic Forces Is a General Endothelial Feature Even OccuringIn Immortalized Cell Lines. Endothelium. 1999; 6(4): 325-334.

23. Duvall C L, Taylor W R, Weiss D, Guldberg R E. Quantitative Microcomputed tomography analysis of collateral vessel development after ischemic injury. Am J Physiol Heart Circ Physiol. 2004; 287 (1): H302-H310.

24. Feldkamp L A, Goldstein S A, Parfitt A M. The direct examination of three dimensional bone architecture *in vitro* by computed tomography. J Bone Miner Res. 1989; 4: 3–11.

25. François Hallouard, NicolasAnton , PhilippeChoquet, André Constantinesco, Thierry Vandamne. Iodinated blood pool contrast media for preclinical X-ray imaging applications - A review. Biomaterials. 2010; 31(24): 1-20.

26. Gantt D G, Kappleman J, Ketcham R A, Alder M E, Deahl T H. Three-dimensional reconstruction of enamel thickness and volume in humans and hominoids. Eur J Oral Sci. 2006; 114(1): 360–364, 375–376 and 382–383.

27. Hainfeld J F, Slatkin D N, Focella T M, Smilowitz H M. Gold nanoparticles: A new X-ray contrast agent. The British Journal of Radiology. 2006;79: 248–253.

28. Hayat M. Positive staining, In: Principle and Techniques of electron microscopy: Biological Applications. Cambridge University Press. 1970; 248-252.

29. Henrik S Thomsen, Peter Marckmann, Vibeke B Logager. Nephrogenic systemic fibrosis (NSF): a late adverse reaction to some of the gadolinium based contrast agents. Cancer Imaging. 2007; 7(1): 130–137.

30. Hiu Yan Yeung, Ling Qin, Kwong Man Lee, Kwok Sui Leung, Jack Chun Yiu Cheng. Quantification of Porosity, Connectivity and Material Density of Calcium Phosphate ceramic Implants using Micro computed Tomography. In. Advanced Bioimaging Technologies in Assessment of the Quality of Bone and Scaffold Materials: Techniques and Applications. Ling Qin, Harry K Genant, James F Griffith and Kwok-Sui Leung (eds). New York: Springer; 2007: 417-429.

31. Hounsfield G N. EMI scanner. Proc. Roy. Soc. Lond. B. Biol. Sci. 1977; 195: 281–289.

32. Hua He, Chao Xie and Jicun Ren. Nonbleaching Fluorescence of Gold Nanoparticles and Its Applications in Cancer Cell Imaging._Anal. Chem. 2008; 80 (15): 5951–5957.

33. Ian A Cunningham, Philip F Judy. Computed tomography. In. Karen M Mudry, Robert Plonsey and Joseph D Bronzino (eds). Principle and Applications in engineering Series-Biomedical Imaging. New York: CRC Press; 2003: 1-16.

34. Jennifer B Hall, Marina A Dobrovolskaia, Anil K Patri, and Scott E McNeil. Characterization of Nanoparticles for Therapeutics: Physicochemical Characterization. Nanomedicine. 2007; 2(6): 789-803.

35. Jirun Sun, Rui Fang, Nancy Lin, Naomi Eidelman, Sheng Lin Gibson. Nondestructive quantification of leakage at the tooth composites interafce and its correlation with material performance parameters. Biomaterials. 2009; 30: 4457-4462.

36. Kaeuis A. Faraj, Vincent M J I. Cuijpers, Ronnie G Wismans, X. Frank Walboomers, John A Jansen, Toin H Van Kuppevelt, Willeke F Daamen. Micro-Computed Tomographical Imaging of Soft Biological Materials Using Contrast Techniques. Tissue engineering. 2009; 15(3): 493-451.

37. Kak A C, Slaney M. Principles of Computerized Tomographic Imaging. The Institute of Electrical and Electronics Engineers, Inc. 1988 New York.

38. Ketcham R A, Carlson W D. Acquisition, optimization and interpretation of X-ray computed tomographic imagery: applications to the geosciences. Computers & Geosciences. 2001; 27(4): 381-400.

39. Kiernan J A. Histological and histochemical methods: Theory and Practice. Oxford: Pergamon Press; 1990.

40. Kim I, Paik K S, Lee S P. Quantitative evaluation of the accuracy of micro-computed tomography in tooth measurement. Clin Anat. 2007; 20(1): 27–34.

41. Krause W, Gerlach S, Muschick P. Prevention of the hemodynamic effects of iopromide-carrying liposomes in rats and pigs. Invest Radiol. 2000; 35: 493-503.

42. Kumar S, Aaron J, Sokolov K. Directional conjugation of antibodies to nanoparticles for synthesis of multiplexed optical contrast agents with both delivery and targeting moieties. Nature Protocols. 2008; 3: 314 - 320.

43. Landis E, Keane D, Shah L. Microtomography of Cement-Based Materials. National Science Foundation. Available: http://www.umeciv.maine.edu/landis/XMT/Default.htm.

44. Linda C Sawyer, David T Grubb, Gregory F Meyers. Polymer microscopy, Springer. 2008; 175-177.

45. Lindblom K. On microtomography. Acta Radiol. 1954; 42(6): 465-468.

46. Ling Qin, Ge Zhang, Hui Sheng, James F Griffth, Ka Wai Yeung, Kwok-Sui Leung. Contrast Enhanced MRI and Micro-CT Adopted for evaluation of a Lipid lowering and anti coagulant Herbal Epidemium-Derived Phytoestrogenic extract for prevention of Steroid Associated Osteonecrosis. In. Ling Qin, Harry K Genant, James F Griffith, Kwok -Sui Leung (eds), Advanced Bioimaging Technologies in Assessment of the Quality of Bone and Scaffold Materials: Techniques and Applications. New York: Springer; 2007: 417-429.

47. Martin Stauber, Ralph Müller. Micro-Computed Tomography: A Method for the Non-Destructive Evaluation of the Three-Dimensional Structure of Biological Specimens. In. Methods in Molecular Biology- Osteoporosis Methods and Protocols. Jennifer J. Westendorf. New York: Springer; 2008: 273-292.

48. Mario Gössl, Michael D Bentley, Lilach O Lerman. Review – 3D Micro-CT Imaging of Renal Micro-Structural Changes. Nephron Clin Pract. 2006; 103: 66 –70.

49. Michael D Bentley, Maria C Ortiz, Erik L Rittman, J Carlos Romero. The use of microcomputed tomography to study microvasculature in small rodents. Am J Physiol Regulatory Integrative Comp Physiol. 2002; 282: R1267–R1279.

50. Michael V Swain, Jing Xue. State of the Art of Micro-CT Applications in Dental Research. Int J Oral Sc. 2009; 1(4): 177–188.

51. Müller R, Rüegsegger P. Morphological validation of the 3D structure of non-invasive bone biopsies. Abstracts 10th Int. Workshop on Bone Densitometry. Bone Miner.1994; 25: 8.

52. Nora De Clerck, Andrei Postnov. High Resolution X-Ray Micro tomography: Applications in Biomedical Research. In. Vasilis Ntziachristos, Anne Leroy Willing , Betrand Tantian (eds). Textbook of in vivo imaging in vertebrates. New York: John Wiley & Sons Ltd; 2007: 58-77.

53. Oded Rabin, J Manuel Perez, Jan Grimm, Gregory Wojtkiewicz, Ralph Weissleder. An X-ray computed tomography imaging agent based on long-circulating bismuth sulphide nanoparticles. Nature materials. 2006; 5: 118-123.

54. Phillip H Kuo, Emanuel Kanal, Ali K Abu-Alfa, Shawn E Cowper. Gadolinium-based MR Contrast Agents and Nephrogenic Systemic Fibrosis. Radiology. 2007; 242: 647-649.

55. Raphael Levy, Umbreen Shaheen, Yann Cesbron, Violaine See. Gold nanoparticles delivery in mammalian live cells: a critical review. Nano Reviews. 2010; 1: 4889.

56. Richard L Ehman, William R Hendee, Michael J Welch, N Reed Dunnick, Linda B Bresolin, Ronald L Arenson, Stanley Baum, Hedvig Hricak, James H Thrall. Blueprint for Imaging in Biomedical Research. Radiology. 2007; 244: 12–27.

57. Robert E Guldberg, Craig L Duvall, Alexandra Peister, Megan E Oest, Angela SP Lin, Ashley W Palmer, Marc E Levenston. 3D imaging of tissue integration with porous biomaterials. Biomaterials. 2008; 29(28): 3757-3761.

58. Salome M, Peyrin F, Cloetens P, Odet C, Laval-Jeantet A M, Baruchel J, Span P. A synchrotron radiation microtomography system for the analysis of trabecular bone samples. Med Phys. 1999; 26(10): 2194-2204.

59. Sandra J Shefelbine, Ulrich Simon, Lutz Claes, Andreas Gold, Yankel Gabel, Itabi Bab, Ralph Muller, Peter Augat. Prediction of fracture callus mechanical properties using micro-CT images and voxel-based finite element analysis. Bone. 2005; 36(3): 480-488.

60. Shauna M Dorsey, Sheng Lin-Gibson, Carl G Simon. X-ray microcomputed tomography for the measurement of cell adhesion and proliferation in polymer scaffolds. Biomaterials. 2009; 30(16): 2967-2974.

61. Spanne P. X-Ray-Energy Optimization in Computed Microtomography. Phys Med Biol. 1989; 34(6): 679-690.

62. Srinivasan Mukundan, Ketan B Ghaghada, Cristian T Badea, Chen-Yu Kao, Laurence W Hedlund, James M Provenzale, G Allan Johnson, Emmanuel Chen, Ravi V Bellamkonda, Ananth Annapragada. A Liposomal Nanoscale Contrast Agent for Preclinical CT in Mice. Am.Jour.Rad. 2006; 186: 300–307.

63. Tatiana Nogueira Rocha Clementino Luedemann. Micro-Computed Tomography in caries research. Ph.D. Thesis. 2007; 2-3.

64. Timothy Andrew John Hopper. Quantitative MRI and Micro CT of Bone architecture: Applications and Limitations in orthopedics Ph.D.Thesis. 2005; 64-71.

65. Van Geet M. X-Ray Microfocus Computer Tomography. Katholieke Universiteit. Leuven. 1997 Available:
http://www.kuleuven.be/geology/Fcg/Sediment/Research/maarten/xray.htm.

66. Vasilis Ntziachristos. Fluorescence Molecular Imaging. Annu. Rev. Biomed. Eng. 2006; 8: 1–33.

67. Wolfgang Eck, Gary Craig, Aruna Sigdel, Gerd Ritter§, Lloyd J Old, Laura Tang, Murray F. Brennan, Peter J. Allen and Michael D. Mason. PEGylated Gold Nanoparticles Conjugated to Monoclonal F19 Antibodies as Targeted Labeling Agents for Human Pancreatic Carcinoma Tissue. ACS Nano. 2008; 2(11): 2263–2272.

68. Yiwei Wang, David F Wertheim, Allan S Jones, Allan G A Coombes. Micro-CT in drug delivery. Eur. J. Pharm. Biopharm. 2009; 74: 41–49.

69. Yongping Zhang, Zhongkun He, Shaojing Fan, Kejia He, Chen Li. Automatic BioMedical Thresholding of Micro-CT Trabecular Bone Images. International Conference on Engineering and Informatics. 2008; 2: 23-27.

70. Yu Pan, Sabine Neuss, Annika Leifert, Monika Fischler, Fei Wen, Ulrich Simon, Günter Schmid, Wolfgang Brandau, Willi Jahnen-Dechent. Size-Dependent Cytotoxicity of Gold Nanoparticles. Small. 2009; 3(11): 1941-1949.

71. Zhi-juan Zhang, Chun-xia Wang, Yong Wang, Shu-hua Niu, Chang-gui Lu, De-gang Fu. Fluorescent Property of Gold Nanoparticles with Different Surface Structures. Chin. J. Chem. Phys. 2007; 20(6): 796- 800.

Appendix 1

Appendix I

1. Preparation of PTA stain (1%)

Phosphotungstic acid hydrate – 1 g

Deionised water (DI) -100 ml

1 g of Phosphotungstic hydrate is dissolved in 100ml of DI water. Different concentrations of the staining solutions (1-0.1%) were prepared by diluting it with absolute alcohol. Absolute alcohol was obtained by vacuum distillation using Flash Rota vaporization of rectified spirit (94.68%).

2. Preparation of Chloroauric acid stock solution (12.7mM)

0.025g of gold (III) chloride trihydrate is dissolved in 5 ml of DI water.

3. Preparation of Trisodium citrate solution (38.8mM)

0.1141g of sodium citrate dibasic trihydrate is dissolved in 10 ml of DI water.

4. Preparation of Phosphate Buffered Saline (pH-7.4, 1x)

Sodium chloride (NaCl) – 150 mM

Potassium dihydrogen phosphate (KH_2PO_4) – 1.5 mM

Disodium hydrogen phosphate (Na_2HPO_4) – 10 mM

Distilled water-1000 ml

pH was adjusted using 1M HCl.

5. Preparation of Paraformaldehyde fixative (1%)

Paraformaldehyde- 1 g

PBS (1x) -100ml

1 g paraformaldehyde is added on to 50 ml PBS and 2 drops of 1 M NaOH is added to dissolve the cloudy precipitate. The final volume is made up to 100 ml with PBS.

6. Preparation of MayGrunwald-Giemsa (MGG) stain

May Grunwald solution and Giemsa solution are mixed in the ratio of 4:1 and equal amount of water is added (5 ml).